### UNIVERSIDAD SAN FRANCISCO DE QUITO USFQ

### Colegio de Posgrados

Chiral Induced Spin Selectivity (CISS) in Biological Molecules

Tesis en torno a una hipótesis o problema de investigación y su contrastación

Valeria Bedoya Jiménez

Ernesto Medina, Ph.D. Director de Trabajo de Titulación

Trabajo de titulación de posgrado presentado como requisito para la obtención del título de Magister en Física

Quito, December 22, 2024

# UNIVERSIDAD SAN FRANCISCO DE QUITO USFQ

### COLEGIO DE POSGRADOS

### HOJA DE APROBACIÓN DE TRABAJO DE TITULACIÓN

Chiral Induced Spin Selectivity (CISS) in Biological Molecules

## Valeria Bedoya Jiménez

Dario Niebieskikwiat Nombre del Director del Programa: Título académico: Doctor en Física Director del programa de: Maestría en Física Nombre del Decano del Colegio Académico: Eduardo Alba Título académico: Doctor en Ciencias Matemáticas Decano del Colegio: Colegio de Ciencias e Ingeniería Nombre del Decano del Colegio de Dario Niebieskikwiat Posgrados: Doctor en Física Título académico:

# © DERECHOS DE AUTOR

Por medio del presente documento certifico que he leído todas las Políticas y Manuales de la Universidad San Francisco de Quito USFQ, incluyendo la Política de Propiedad Intelectual USFQ, y estoy de acuerdo con su contenido, por lo que los derechos de propiedad intelectual del presente trabajo quedan sujetos a lo dispuesto en esas Políticas.

Asimismo, autorizo a la USFQ para que realice la digitalización y publicación de este trabajo en el repositorio virtual, de conformidad a lo dispuesto en la Ley Orgánica de Educación Superior del Ecuador.

Quito, December 22, 2024

| Nombre del Estudiante: | Valeria Bedoya Jiménez |
|------------------------|------------------------|
| Código del Estudiante: | 334874                 |
| C.I.:                  | 1718722919             |
|                        |                        |

Lugar y Fecha:

#### ACLARACIÓN PARA PUBLICACIÓN

Nota: El presente trabajo, en su totalidad o cualquiera de sus partes, no debe ser considerado como una publicación, incluso a pesar de estar disponible sin restricciones a través de un repositorio institucional. Esta declaración se alinea con las prácticas y recomendaciones presentadas por el Committee on Publication Ethics COPE descritas por Barbour et al. (2017) Discussion document on best practice for issues around theses publishing, disponible en http://bit.ly/COPETheses.

#### UNPUBLISHED DOCUMENT

Note: The following graduation project is available through Universidad San Francisco de Quito USFQ institutional repository. Nonetheless, this project – in whole or in part – should not be considered a publication. This statement follows the recommendations presented by the Committee on Publication Ethics COPE described by Barbour et al. (2017) Discussion document on best practice for issues around theses publishing available on http://bit.ly/COPETheses.

# Agradecimientos

Agradezco a mis papás y a mis hermanos por apoyarme y estar presentes siempre en todas las etapas de mi vida. Gracias por animarme en los momentos difíciles y, sobre todo, gracias por su amor y entrega incondicional.

También agradezco a mis amigos de la Universidad, siempre nos hemos apoyado mutuamente en este camino y han sido parte indispensable a lo largo de mi carrera. En especial, quiero mencionar a David, mi compañero de todo el pregrado y ahora de la maestría. Ha sido un gran apoyo en todo este proceso.

Quiero agradecer a mi tutor, Ernesto Medina, por su guía y por permitirme ser parte de uno de sus proyectos. Ha sido un verdadero honor empaparme de todo su conocimiento a lo largo de este trabajo.

Por último, quiero agradecer a todos mis profesores de la Universidad que han contribuido a mi formación académica, que me han apoyado y me han ayudado a crecer como persona.

Resumen

La Selectividad de Espín Inducida por Quiralidad (CISS por sus siglas en inglés) es un

fenómeno experimental que se ha documentado de manera detallada, donde moléculas

quirales exhiben polarizaciones electrónicas altas en una configuración de transporte de

dos terminales, proporcionando un recurso prometedor para la espintrónica molecular.

Explicar este efecto ha constituido un desafío teórico, comenzando desde modelos con-

tinuos [1, 2] de estructuras helicoidales, hasta modelos de enlaces fuerte [3, 4, 5, 6] que

implican los orbitales en el transporte. La reciprocidad de Onsager es la principal regla

que rige el transporte en sistemas con simetría de reversión temporal y pocos de los mode-

los propuestos en la literatura cumplen con esta condición [7]. En este trabajo se hace una

evaluación crítica de los modelos orbitales discretos previos y se aborda una propuesta

analítica y numérica que satisface la reciprocidad, y que incluye procesos de decoherencia

como mecanismo de rompimiento de reversibilidad temporal, necesario para la acumu-

lación de espín. Nuestro modelo produce polarizaciones altas dentro de una descripción

realista, tanto de hélices simples como dobles y valida cualitativamente escenarios recientes

establecidos por modelos mínimos de CISS exactamente resueltos.

Palabras clave: CISS, tight-binding, Quiralidad, Polarización de espín

Abstract

Chiraly Induced Spin Selectivity (CISS) is a very well experimentally documented phe-

nomenon, where chiral molecules in a two-terminal transport setup exhibit electron polar-

ization to an extraordinary degree, furnishing a promising resource for molecular spintron-

ics. Explaining this effect has constituted a theoretical challenge, starting from continuous

models [1, 2] of helical structures to tight-binding models [3, 4, 5, 6] that surmise the or-

bitals involved in transport. A major test for two terminal spin selection is Onsager's

reciprocity relations [7], which apply to systems with time-reversal symmetry that very

few of the models in the literature comply with. Here, we discuss a critical assessment of

the previous discrete orbital models and embark on an analytical and numerical proposal

that satisfies reciprocity and includes decoherence processes as sources of time-reversal

symmetry-breaking mechanisms. Our model yields high polarization outputs within a

realistic description of both single and double helices and validates qualitatively recent

scenarios set by exactly solved minimal models of CISS.

Keywords: CISS, tight-binding, Chirality, Spin Polarization

# Contents

| 1  | Intr  | introduction               |           |  |  |  |  |
|----|-------|----------------------------|-----------|--|--|--|--|
|    | 1.1   | Tight-Binding models       | 16        |  |  |  |  |
| 2  | Met   | hods                       | <b>25</b> |  |  |  |  |
|    | 2.1   | The Model                  | 25        |  |  |  |  |
|    | 2.2   | Slater-Koster Terms        | 29        |  |  |  |  |
|    | 2.3   | Landauer Formalism         | 33        |  |  |  |  |
|    | 2.4   | Dephasing                  | 36        |  |  |  |  |
|    | 2.5   | Band Folding               | 40        |  |  |  |  |
| 3  | Res   | ults                       | 42        |  |  |  |  |
|    | 3.1   | Spin Polarization in ssDNA | 42        |  |  |  |  |
|    |       | 3.1.1 Tunneling effect     | 45        |  |  |  |  |
|    | 3.2   | Spin Polarization in dsDNA | 47        |  |  |  |  |
|    |       | 3.2.1 Tunneling effect     | 49        |  |  |  |  |
|    | 3.3   | Band Folding               | 51        |  |  |  |  |
| 4  | Con   | clusions                   | <b>54</b> |  |  |  |  |
|    | 4.1   | Future work                | 55        |  |  |  |  |
| Bi | bliog | rafía                      | 56        |  |  |  |  |

# List of Tables

| 2.1 | Orbital energies of DNA base pairs calculated through tight-binding meth- |    |
|-----|---|----|
|     | ods, as reported in ref. [8]  | 29 |

# List of Figures

| 1.1 | Achiral nanotube   | 16 |
|-----|--|----|
| 1.2 | Conductances and spin polarization reported by Guo-Sun                           | 18 |
| 1.3 | Conductances and spin polarization results of the Guo-Sun model in Kwant.        | 18 |
| 1.4 | Robustness of the spin polarization Guo and Sun's model                          | 20 |
| 1.5 | Robustness of the spin polarization Guo and Sun's model II                       | 20 |
| 1.6 | Model of dsDNA of the Guo and Sun's model  | 22 |
| 1.7 | Guo and Sun results for dsDNA  | 22 |
| 1.8 | Charge transmission in the $(G:C)-(T:A)_j(G:C)_3$ sequence                       | 24 |
| 2.1 | Slater Koster terms and helix with s and p orbitals                              | 25 |
| 2.2 | Complete Hamiltonian structure of the DNA  | 28 |
| 2.3 | Energy scheme in the molecule and the leads and diagram of the connection        |    |
|     | between the leads and the system's orbitals                                      | 35 |
| 3.1 | Conductance and spin polarization in ssDNA                                       | 43 |
| 3.2 | Average spin polarization in ssDNA as a function of a) number of turns           |    |
|     | (n) b) the coupling strength of the dephasing probe to the system                | 44 |
| 3.3 | Spin polarization without tilt   | 44 |
| 3.4 | Energy scheme with barrier and average spin polarization in ssDNA as a           |    |
|     | function of barrier intensity  | 45 |
| 3.5 | Spin polarization as a function of the spin-orbit strength and the dephasing     |    |
|     | coupling strength (a) without a barrier (b) with a barrier intensity of 1 $eV$ . | 46 |
| 3.6 | Spin polarization in ssDNA below and above the barrier                           | 46 |
| 3.7 | Conductance in dsDNA   | 48 |

| 3.8  | Spin polarization (above panel) and conductance (below panel) in a DNA        |    |
|------|---|----|
|      | toy model of 3 pair bases as a function of the injection energy of the leads. | 48 |
| 3.9  | Averaged spin polarization in DNA in as a function of (a) number of turns     |    |
|      | (n) (b) the coupling strength of the dephasing probe to the system            | 49 |
| 3.10 | Energy scheme with barrier and average spin polarization in dsDNA as a        |    |
|      | function of barrier intensity   | 49 |
| 3.11 | Spin polarization in dsDNA below and above the barrier                        | 50 |

# Chapter 1

# Introduction

Chiral Induced Spin Selectivity (CISS) refers to the quantum mechanical phenomenon where chiral molecules act as spin filters, enabling spin-polarized electron transport [9]. The history of CISS begins with the recognition of spin activity in ferromagnetic materials, an essential aspect of spintronics. Spin-polarized transport was first described by Mott in 1936, who proposed that the resistance of ferromagnetic materials could be explained by considering the separate behaviors of spin-up and spin-down electrons, leading to spin-polarized currents [10, 11]. This idea laid the foundation for the control of the spin and the development of devices like spin valves, which paved the way for further research into spin-polarized electron transport in other systems, including chiral materials [12].

The first proposal of the relation between chirality and spin selection was made by Farago [13], who surmised that point chiral molecules such as amino acids, when scattering electrons, could yield an angle-dependent spin polarization. This proposal was later measured by Kessler [14] for point chiral molecules in the gas phase. The spin effect was small  $(10^{-4}\%)$  and this was only achieved after attaching heavy atoms to the chiral Camphor molecules. Thompson and Blum [15] extensively developed the scattering theory of chiral units, demonstrating chiral-dependent spin polarization in the Born scattering formalism.

For some years there was little interest in the small spin polarizing effect of chiral molecules until the first experimental observation of the CISS effect came in 1999 [16]. It was demonstrated that spin-polarized electrons can be filtered through chiral molecules,

producing asymmetries significantly larger than those observed in the gas phase or even in ferromagnets [16]. Since this discovery, numerous experiments have validated this phenomenon across various chiral systems, including oligopeptides, helicenes, proteins, chiral perovskites, and dichalcogenide crystals [17]. Additionally, several advanced measurement techniques have been developed to study this effect [9]. The CISS effect establishes a fundamental connection between molecular chirality and electron spin, with far-reaching implications for spin-based technologies and the understanding of life's homochiral nature [18, 19, 20].

CISS is commonly measured using techniques such as photoelectron spectroscopy, Mott polarimetry, conductive probe atomic force microscopy (mc-AFM), and scanning tunneling microscopy (STM), all of which provide valuable insights into the spin-selective behavior of electron transport through chiral materials [9]. However, to understand spin polarization, it is essential first to analyze the fundamental behavior of electrons in chiral molecules.

Ref. [21] explored long-distance electron transfer in DNA, focusing on charge transport rates and efficiency under various conditions. Their findings revealed that electron transfer primarily occurs via a multistep hopping mechanism, with guanine and, in some sequences, adenine serving as charge carriers. Similarly, ref. [22] examined electron transport in non-electron transfer proteins, challenging the notion that these proteins act as insulators. The study measured single-molecule conductance, the energy of resonant electronic states, and conductance variations related to protein conformations. It demonstrated that non-electron transfer proteins exhibit significant conductivity, comparable to bacterial filaments, with transport mediated through resonant states involving aromatic residues such as tyrosine and tryptophan.

Among the types of chirality, axial or helical chirality has the most pronounced effect on spin selectivity in organic systems. For example, mc-AFM measurements showed spin polarizations as high as 57% in double-stranded DNA, while single-stranded DNA exhibited no significant spin polarization [23]. Nevertheless, experiments using ultraviolet photoelectron spectroscopy (UPS) have reported spin polarizations in single-stranded

DNA chelated with Hg [24], indicating the influence of external factors on spin selectivity. Studies in proteins as the experiment of ref. [25] investigated spin polarization in electron transfer through Photosystem I (PSI) using a spintronic device. Experiments on several classes of helicenes [26, 27, 28] and polymers [29, 30] have also shown that these materials are significant sources of spin selectivity.

Most experiments have explored the response of spin polarization under varying parameters. A strong dependence between molecular length and spin polarization has been demonstrated, with several studies showing that spin polarization increases with the length of the molecule [23, 31, 32]. Ref. [25] revealed that spin polarization peaks at room temperature, with electron spins aligned parallel to their momentum, but decreases sharply below 150 K, disappearing entirely at lower temperatures. These findings high-light the temperature-dependent nature of spin polarization, driven by thermal energy and molecular dynamics. However, studies have also shown that heterogeneous or structurally disordered systems exhibit poor or negligible spin polarization [33, 34, 35].

According to theoretical models explaining CISS, spin-orbit coupling (SOC) has been established as the primary mechanism for spin activity in chiral systems [13, 14, 15]. However, it has been demonstrated that SOC alone cannot generate spin polarization in non-helical systems. At the same time, the absence of SOC could be argued with some angular momentum transfer mechanisms to produce spin polarization [36]. The great variety of experimental findings now available challenge the previous minimal ingredients. For instance, theoretical studies have shown that orbital overlap and hydrogen bonding networks can modulate SOC [37], emphasizing the importance of controlling structural variations when evaluating SOC's role. Furthermore, experiments on metallopeptides have shown that incorporating a paramagnetic material results in higher spin polarization than using a diamagnetic one, with the magnetic properties overriding the influence of SOC [38]. To clarify the relationship between SOC and spin polarization, more detailed experiments are needed to isolate SOC's effects from other contributing factors.

Significant efforts have been made to develop effective models that reproduce experimental results using experimentally measurable parameters and enhance the understanding of CISS. These approaches are typically categorized into three main groups: hydrodynamic or continuum models [39, 40, 41], tight-binding frameworks [3, 4, 42, 43], and ab initio methods such as density functional theory (DFT) [44, 45]. While many theoretical models successfully report spin polarization, some approaches raise concerns: (i) SOC is often introduced as an adjustable parameter that must be tuned to unrealistically high values to match experimental spin polarization results, and (ii) DFT models frequently report spin polarization in two-terminal setups, which violates Onsager's reciprocity relations.

The objective of this work is to address the shortcomings of current models in understanding spin selectivity by constructing a tight-binding model that incorporates the following key characteristics:

- 1. Orbital involvement in transport.
- 2. Intrinsic SOC as a source of spin activity.
- 3. Chirality as a source of space inversion asymmetry.
- 4. Couplings to the environment as a source of time-reversal symmetry breaking.

In the initial stage of this work, tight binding models from the literature are addressed. Some results are reproduced to validate the computational methods used and serve as a foundation for our model development. In the methods section, the s- and p-orbital Hamiltonian is calculated considering the geometry of the orbitals in the helix's base. The Landauer formalism is utilized for analyzing electron transmission and spin polarization. The model did not exhibit spin polarization in a two-terminal setup in accordance with the Onsager reciprocity. The results provide a comprehensive characterization of electron behavior in two systems: single-stranded DNA (ssDNA) and double-stranded DNA (dsDNA).

### 1.1 Tight-Binding models

We first analyzed existing tight-binding models from the literature and validated our computational methods by reproducing their results. Two significant studies were selected for comparison: ref. [6], where chirality is introduced through asymmetrical connections to input and output leads, and ref. [4], which explores spin polarization in single-stranded (ssDNA) and double-stranded DNA (dsDNA). These models are among the most robust in the literature, successfully describing spin transport in chiral molecules.

#### Achiral Nanotubes

To validate our approach, we used the Kwant framework [46] to replicate the results from the selected studies. In ref. [6], where an achiral nanotube was modeled, and mirror asymmetry was introduced by connecting the output lead to a site different from that of the input lead. This modification caused the two-terminal system to behave like a chiral molecule.

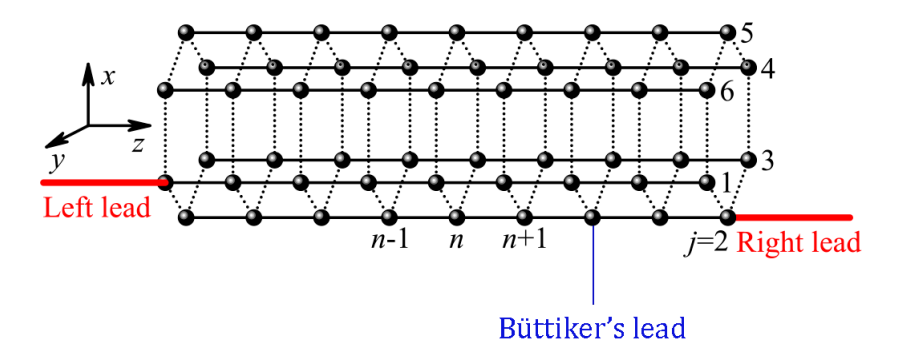


Figure 1.1: Representation of the achiral nanotube in the model of Guo-Sun with one Büttiker's lead connected to a site.

The Hamiltonian that describes the system has the form:

$$\mathcal{H} = \mathcal{H}_0 + \mathcal{H}_{el} + \mathcal{H}_d, \tag{1.1}$$

where  $\mathcal{H}_0 = \mathcal{H}_{nt} + \mathcal{H}_{SO}$ ,  $\mathcal{H}_{nt} = \hat{p}^2/2m + V$  describes the kinectic and potential energies of the electron, and  $\mathcal{H}_{SO} = (\hbar/4m^2c^2)\nabla V(\hat{\sigma}\times\hat{p})$  is the SOC term,  $\hat{p}$  is the momentum operator, m is the electron effective mass,  $\hbar$  is the Planck constant, c is the speed of light, and  $\hat{\sigma} = (\sigma_x, \sigma_y, \sigma_z)$  with  $\sigma_{x,y,z}$  being the Pauli's matrices.

The procedure to discretize the Hamiltonian follows the method of finite differences, detailed in 4.1. The final tight-binding Hamiltonian has the form:

$$H_{0} = \sum_{j=1}^{J} \left[ \sum_{n=1}^{N} \epsilon_{jn} c_{jn}^{\dagger} c_{jn} + \sum_{n=1}^{N-1} c_{jn}^{\dagger} (t_{\parallel} + 2is\sigma_{j}) c_{j,n+1} + \sum_{n=1}^{N} c_{jn}^{\dagger} (t_{\perp} + 2i\mu\sigma_{z}) c_{j+1,n} + H.c. \right],$$

$$(1.2)$$

here  $\{c_{jn}^{\dagger}, c_{jn}\}$  are the creation and annihilation operators on the site  $\{j, n\}$  in the nanotube, J is the number of chains, N is the length of the nanotube,  $\epsilon_{jn}$  is the potential energy,  $t_{\parallel}$  ( $t_{\perp}$ ) is the intrachain (interchain) hopping integral, and s ( $\mu$ ) is the intrachain (interchain) SOC parameter;  $\sigma_{j} = \sigma_{x} \sin \phi_{j} - \sigma_{y} \cos \phi_{j}$  and  $\phi_{j}$  is the azimuth angle of the site in cylindrical coordinates. For the numeric factors used in the simulations, see ref. [6].

Note that prefactor in the SOC term  $-i\hbar^2/4m^2c^2\nabla V(\epsilon_{ijk}\sigma_j\partial_k)$  is on the order of  $10^{-8}~eV/N$ . To generate SOC intensity of the order of meV, it would require  $\nabla V = 10^5~N/C$  corresponding to an extraordinarily high electric field for molecular systems under normal conditions.

By Onsager's reciprocity relations, the model did not exhibit spin polarization in a twoterminal setup. A third probe (Büttiker's lead) was incorporated into the system to break the time-reversal symmetry and achieve spin polarization. The resulting spin polarization depended not only on the positions of the magnetic electrodes but also on the location where the third probe was connected. This dependence arises from the asymmetries induced by Büttiker's lead, which affected the system's chirality. Furthermore, when only one decoherence lead was attached, the robustness of spin polarization was influenced by the site of connection due to variations in the wave function amplitudes along the nanotube. This observation was confirmed by plotting the local density of states (LDOS) along the nanotube, showing that sites with low LDOS were suboptimal for introducing decoherence.

The complete model was subsequently tested. Initially, the conductance and spin polarization were evaluated for a nanotube with J=6 chains and N=20 sites per

chain. Decoherence leads were connected to all sites in the system to ensure that mirror asymmetries were solely caused by the input and output terminals. In the figures, j denotes the site where the output lead is connected, while the input lead is fixed at  $\{j=1,n=1\}$ . Refer to the original reference for a complete description of the parameters used.

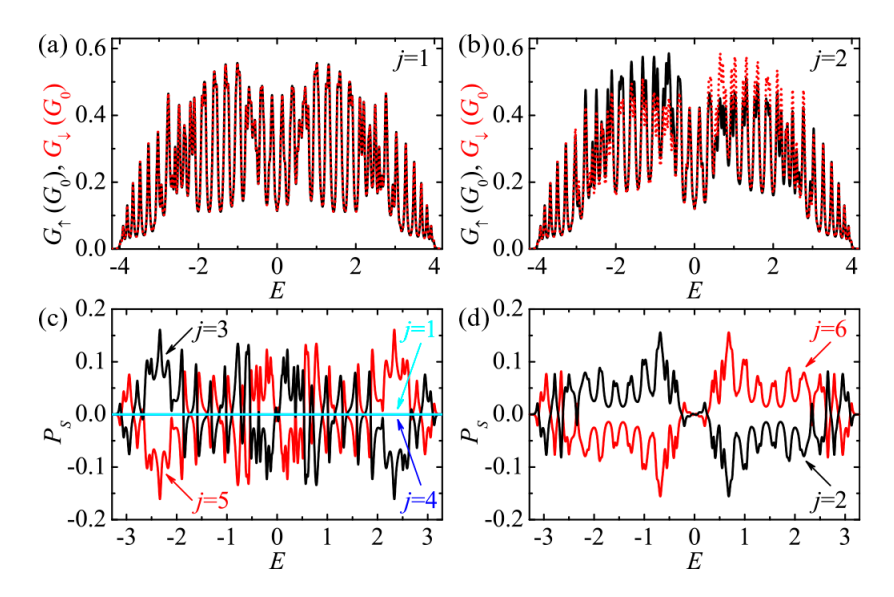


Figure 1.2: Conductances and spin polarization reported by Guo-Sun.

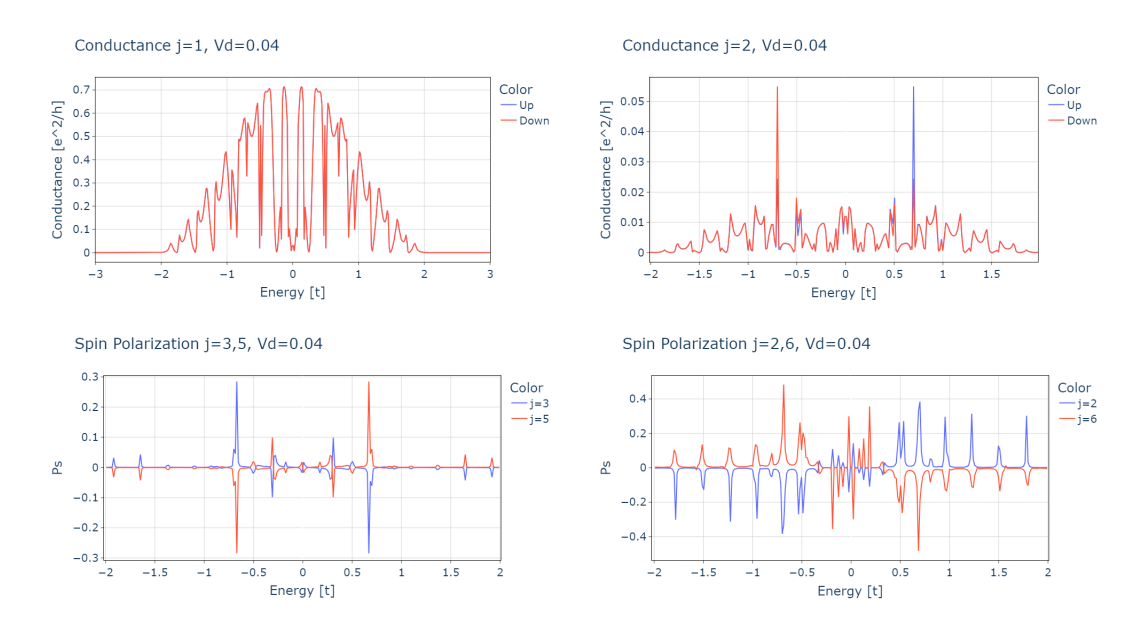


Figure 1.3: Conductances and spin polarization results of the Guo-Sun model in Kwant.

The findings contrast with the results reported by Guo and Sun in terms of the amplitudes of both conductance and spin polarization. For the achiral case (j = 1), the conductance in the Kwant model exceeds 0.7, whereas the reference reported conductances

below 0.6. This discrepancy is even more pronounced in the chiral case j = 2, where the reference values are approximately 10 times greater than the conductance amplitudes obtained in the Kwant model.

The graphs in Figure 1.2 demonstrate the chiral nature of the nanotube as determined by the positions of the leads. For example, Ps(j=2)=-Ps(j=6) because these configurations are mirror images, a property that is independent of the model parameters. A similar relationship is observed for j=3 and j=5. While the Kwant model accurately captures this behavior, discrepancies in conductance values remain. Additionally, the spin polarization values reported in the original study are relatively large, with maximum values of 16% for (j=3,j=5) and 15% for (j=2,j=6). In contrast, the reproduced model yields significantly higher spin polarization maximums, approximately  $\sim 30\%$  and  $\sim 45\%$ , respectively.

It is also noteworthy that the curves are symmetric about the line E=0: The conductances satisfy the relation  $G_{\uparrow}(E)=G_{\downarrow}(-E)$ , while the spin polarization follows  $P_s(E)=-P_s(-E)$ . This symmetry arises from a form of electron-hole symmetry in the system. Specifically, the Hamiltonian in equation 1.2 is invariant under the transformation  $c_{jn\uparrow} \to (-1)^{j+n} c_{jn\downarrow}^{\dagger}$  and  $c_{jn\downarrow} \to (-1)^{j+n+1} c_{jn\uparrow}^{\dagger}$ . However, this electron-hole-type symmetry is broken when J is odd. Refer to Appendix 4.1 for a demonstration of this symmetry.

Spin polarization depends on the coupling of Büttiker's leads to the system ( $\Gamma_d$ ) and the strength spin-orbit coupling (s). The robustness of spin polarization was evaluated by varying these parameters, as described in the reference study. For dephasing, the results confirm that spin polarization increases with higher dephase coupling but decreases at large values of  $\Gamma_d$ . This reduction occurs because strong electron-electron and electron-phonon interactions significantly interfere with electron transmission in the two-terminal setup. The spin polarization as a function of the spin-orbit coupling strength (s) shows significant discrepancies between the model reproduced in Kwant and the original results reported by Guo and Sun. According to the reference, even spin polarization remains noticeable at the smallest value of s = 0.002, with amplitudes around  $\sim 10\%$ . In contrast, the Kwant model produces zero amplitudes for this value of s. As s increases, the spin

polarization also rises in both cases, reaching a maximum of 75 % in the Kwant model and 15 % in the original model.

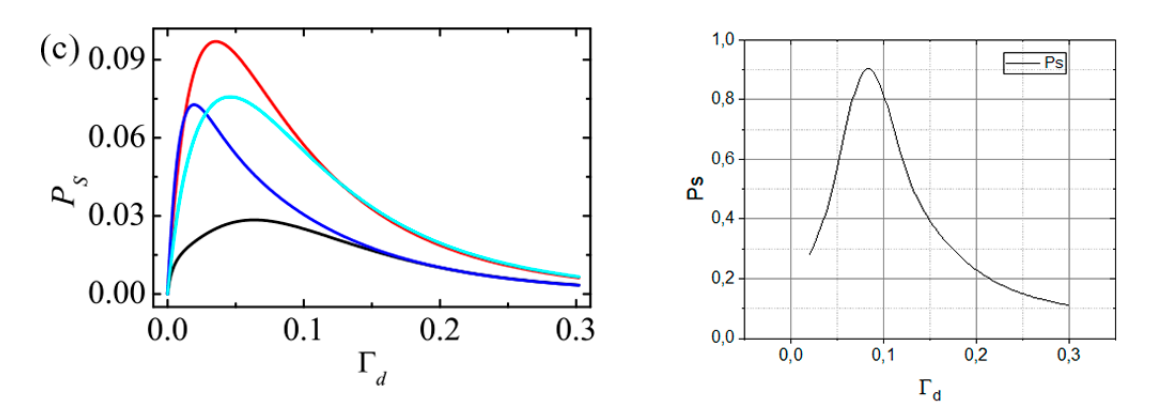


Figure 1.4: (Left) Robustness of the spin polarization reported by Guo and Sun vs. the dephase coupling in the Anderson disorder. (Right) Spin polarization vs. the dephase coupling in the reproduced model in Kwant.

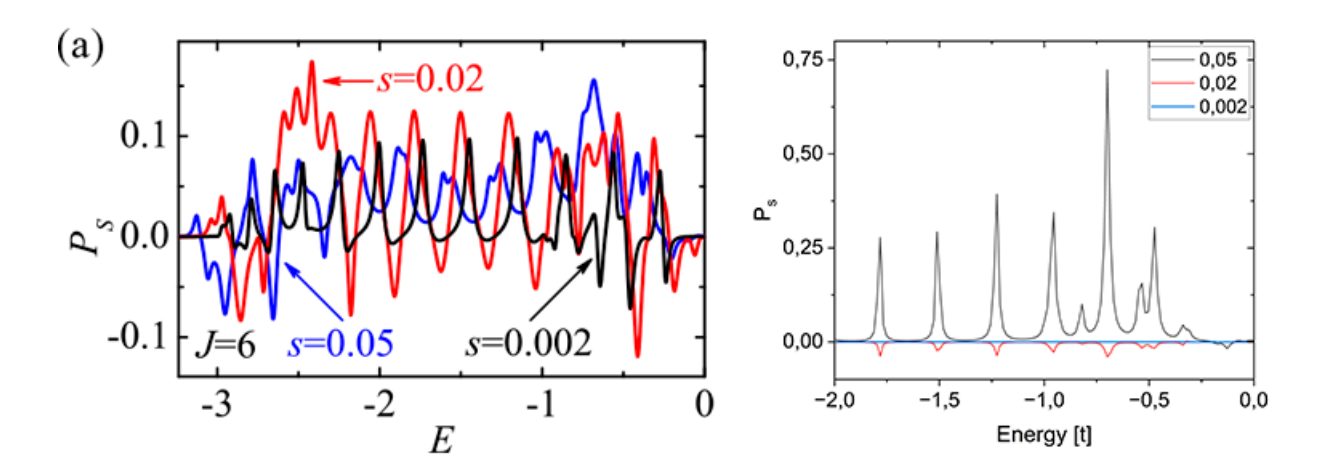


Figure 1.5: (Left) Robustness of the spin polarization reported by Guo and Sun vs. the spin-orbit coupling strength s in the Anderson disorder. (Right) Spin polarization vs. the spin-orbit coupling strength in the reproduced model in Kwant.

#### ssDNA and dsDNA

The study in ref. [4] investigated spin polarization in single-stranded (ssDNA) and double-stranded DNA (dsDNA). No spin polarization was reported for ssDNA, and the analysis focused entirely on dsDNA. Interestingly, a subsequent study by the same authors introduced interactions with additional nearest neighbors and reported spin polarization in

ssDNA [5]. However, the observed spin polarization in ssDNA was approximately 10<sup>-5</sup> which is four orders of magnitude lower than the spin polarization typically observed in dsDNA. Here, it is only discussed the results of the first work. The Hamiltonian describing the system is:

$$\mathcal{H} = \mathcal{H}_{DNA} + \mathcal{H}_{lead} + \mathcal{H}_c + \mathcal{H}_{SO} + \mathcal{H}_d. \tag{1.3}$$

$$\mathcal{H}_{DNA} = \sum_{n=1}^{N} \left[ \sum_{j=1}^{2} (\epsilon_{jn} c_{jn}^{\dagger} c_{jn} + t_{jn} c_{jn}^{\dagger} c_{jn+1}) + \lambda_n c_{1n}^{\dagger} c_{2n} + H.c. \right], \tag{1.4}$$

where N is the DNA length,  $c_{jn}^{\dagger} = (c_{jn\uparrow}^{\dagger}, c_{jn\downarrow}^{\dagger})$  the creation operator of the spinor at the nth site of the jth chain of the dsDNA,  $\epsilon_{jn}$  the on-site energy,  $t_{jn}$  is the intrachain coupling and  $\lambda_n$  is the interchain coupling.

$$\mathcal{H}_{lead} + \mathcal{H}_c = \sum_{k,\beta(\beta=L,R)} [\epsilon_{\beta k} a^{\dagger}_{\beta k} a_{\beta k} + t_{\beta} a^{\dagger}_{\beta k} (c_{1n_{\beta}} + c_{2n_{\beta}}) + H.c.], \tag{1.5}$$

describe the left and right nonmagnetic leads and the couplings between the leads and de dsDNA,  $n_L = 1$  and  $n_R = N$ . The spin-orbit term appears in the same form as in the previous case. The potential V has only a radial component, as the effects are more significant in that direction. Considering charge propagation along a single helical chain of the dsDNA, the momentum is expressed as  $\hat{p} = \hat{p}_{\parallel} \hat{l}_{\parallel}$  where  $\hat{l}_{\parallel}$  is the unit vector in the direction of the helical chain. This reduces the spin-orbit coupling to:

$$\mathcal{H}_{SO} = \sum_{i,n} i t_{SO} c_{jn}^{\dagger} [\sigma_n^j + \sigma_{n+1}^j] c_{jn+1} + H.c.$$
 (1.6)

where  $t_{SO} = \frac{\hbar^2}{4m^2c^2l_a}$ ,  $\sigma_{n+1}^j = \sigma_x \sin(n\Delta\phi)\sin\theta + \sigma_y \cos(n\Delta\phi)\sin\theta + \sigma_z \cos\theta$  with  $\theta$  is the helix angle and  $\Delta\phi$  is the angle between successive base pairs. The interchain SOC has been neglected because it is very small.

The decoherence effects are introduced through the Hamiltonian:

$$\mathcal{H}_d = \sum_{j,n,k} (\epsilon_{jnk} a_{jnk}^{\dagger} + t_d a_{jnk}^{\dagger} c_{jn} + H.c.), \tag{1.7}$$

where  $a^{\dagger}_{jnk}=(a^{\dagger}_{jnk\uparrow},a^{\dagger}_{jnk\downarrow})$  is the creation operator for the virtual lead, and  $t_d$  represents

the coupling strength between the system and the virtual lead. The term  $\epsilon_{jnk}$  denotes the energy of the states in the virtual lead.

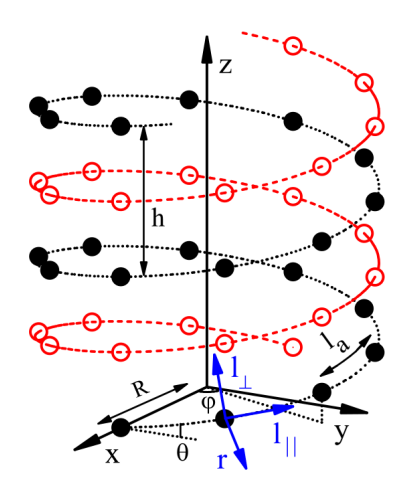


Figure 1.6: Model of dsDNA of the Guo and Sun's model.

The comparison of this model and the Kwant simulation presents the same discrepancies that the model of the achiral nanotubes. The results in Figure 1.7(a) depict the conductance and spin polarization from the original model. Two distinct conductance peaks are observed near energies -0.25 and 0.5 that are reproduced with high fidelity by Kwant in Figure 1.7 (b). The spin polarization reaches  $\sim 30\%$  in the original model, compared to just 2% in the Kwant simulation.

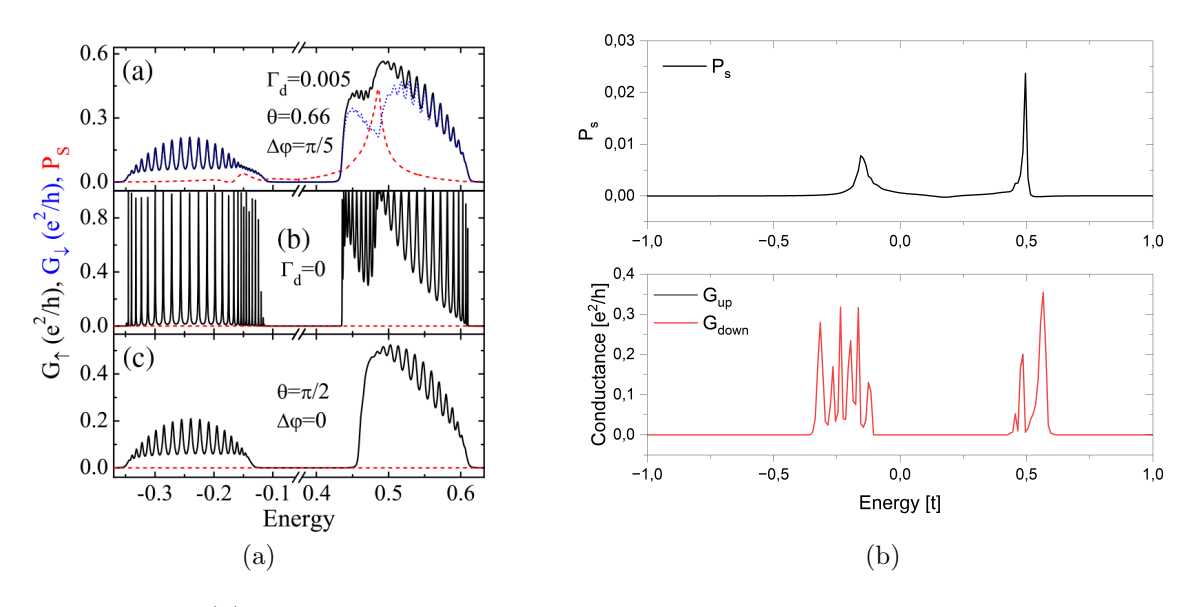


Figure 1.7: (a) Top panel: Conductance and spin polarization in dsDNA in the Guo and Sun's model as a function of the injection energy. Half panel: without decoherence. Bottom panel: without helicity (b) reproduced model in Kwant.

Note that, in both cases—achiral nanotubes and dsDNA—there is no spin polarization in the absence of decoherence or spatial chirality ( $\phi = 0$ ). These findings emphasize that spatial asymmetry, the decoherence introduced by Büttiker's leads, and the presence of spin-orbit coupling are all critical components for achieving spin accumulation in these models.

A barrier was introduced into both systems to analyze its effect on spin polarization. Spin polarization was enhanced when the injection energy was below the site energies of the molecules, consistent with the findings in ref. [47]. Further details on the tunneling effect in spin transport will be discussed in our model.

#### Charge Transfer in DNA

The model in ref. [3] analyzes the charge transfer in DNA, including the heterogeneity of the site energies given the nucleobases in the DNA sequence. This paper presents a ladder model based on a nearest-neighbor tight-binding framework to describe distance-dependent charge transport in DNA. The model's Hamiltonian is introduced, and the transmission function is analyzed to calculate DNA conductance, aiming to reproduce and expand upon the Wang-Chakraborty model [48].

The model is described by the Hamiltonian:

$$\mathcal{H}_{S1} = \epsilon_G b_1^{\dagger} b_1 + \sum_{i=n-2}^{n} \epsilon_G b_i^{\dagger} b_i + \sum_{i=2}^{j+1} \epsilon_i b_i^{\dagger} b_i + t_{\parallel} \sum_{i=1}^{n-1} [b_i^{\dagger} b_{i+1} + H.c.]$$
 (1.8)

$$\mathcal{H}_{S2} = \epsilon_C c_{n+1}^{\dagger} c_{n+1} + \sum_{i=N-2}^{N} \epsilon_C c_i^{\dagger} c_i + \sum_{i=n+2}^{n+j+1} \epsilon_i c_i^{\dagger} c_i + t_{\parallel} \sum_{i=n+1}^{N-1} [c_i^{\dagger} c_{i+1} + H.c.]$$
 (1.9)

$$\mathcal{H}_{S1-S2} = t_{\perp} \sum_{i=1}^{n} [b_i^{\dagger} c_i + H.c.], \tag{1.10}$$

where  $b_i^{\dagger}$  is the creation operator in the ith site of the first strand,  $c_i^{\dagger}$  is the creation operator in the ith site of the second strand,  $t_{\parallel}$  and  $t_{\perp}$  are the intrastrand hopping and interstrand hopping respectively. The on-site energies correspond to  $\epsilon_G = 7.75 \ eV$ ,  $\epsilon_C = 8.87 \ eV$ ,  $\epsilon_T = 9.14 \ eV$ ,  $\epsilon_A = 8.24 \ eV$ . The sequence has the form  $(G:C) - (T:A)_j - (G:C)_3$ .

The study reveals a transition from tunneling-dominated, exponential distance-dependent

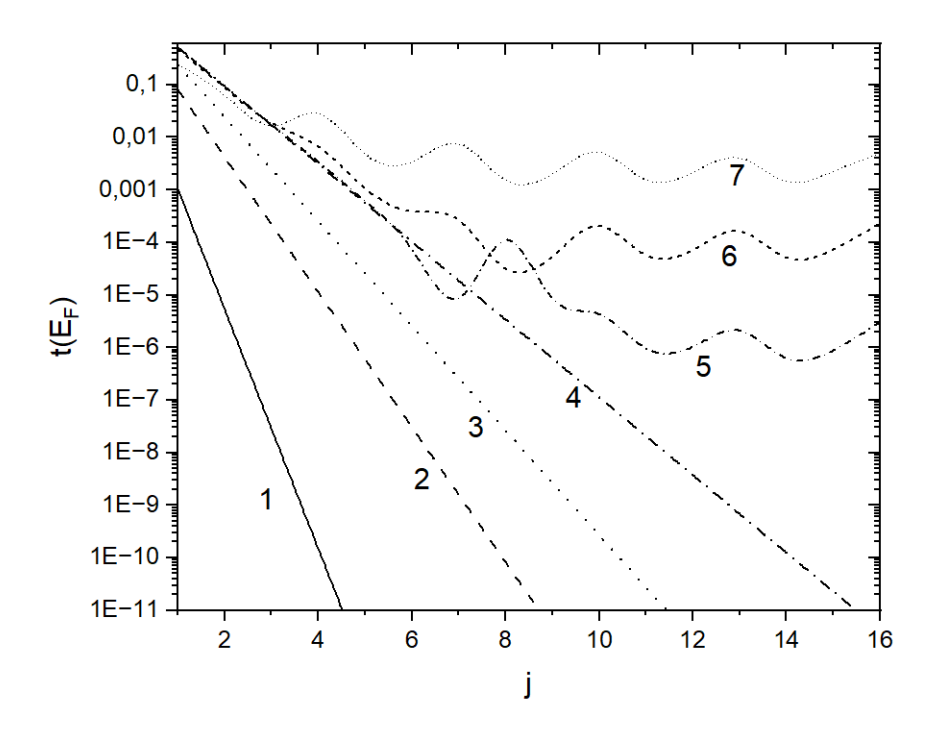


Figure 1.8: Reproduced model in Kwant. Transmission at Fermi's energy as a function of the number of A-T base pair in the DNA model for different intrastrand hopping integrals  $t_{\parallel}$  (1-0.1 eV, 2-0.3 eV, 3-0.4 eV, 4-0.5 eV) with ( $t_{\perp}=0$ ) and for various values of the interstrand hopping  $t_{\perp}$  (5-0.01 eV, 6-0.03 eV, 7-0.07 eV) at fixed  $t_{\parallel}=0.5$  eV. The coupling between the system and the leads was set at 1.5 eV and the coupling between the lead's sites was fixed at 5 eV.

transport to nearly length-independent behavior as electronic coupling parameters increase. For single-stranded DNA, transport follows a tunneling mechanism, whereas in, double-stranded DNA, coherent tunneling occurs through bridge states formed by  $\pi$ - $\pi$  interactions between complementary nucleobases. The intrastrand and interstrand hopping integrals significantly influence this transition, with stronger coupling enhancing electronic state delocalization and promoting band-like transport. Additionally, asymmetric DNA-electrode coupling alters conductance and transport pathways by modifying the delocalization of electronic states. At finite temperatures, coherent tunneling through extended electronic states leads to nearly distance-independent conductance for longer bridges, highlighting the importance of coupling and environmental conditions in DNA charge transport.

# Chapter 2

# Methods

### 2.1 The Model

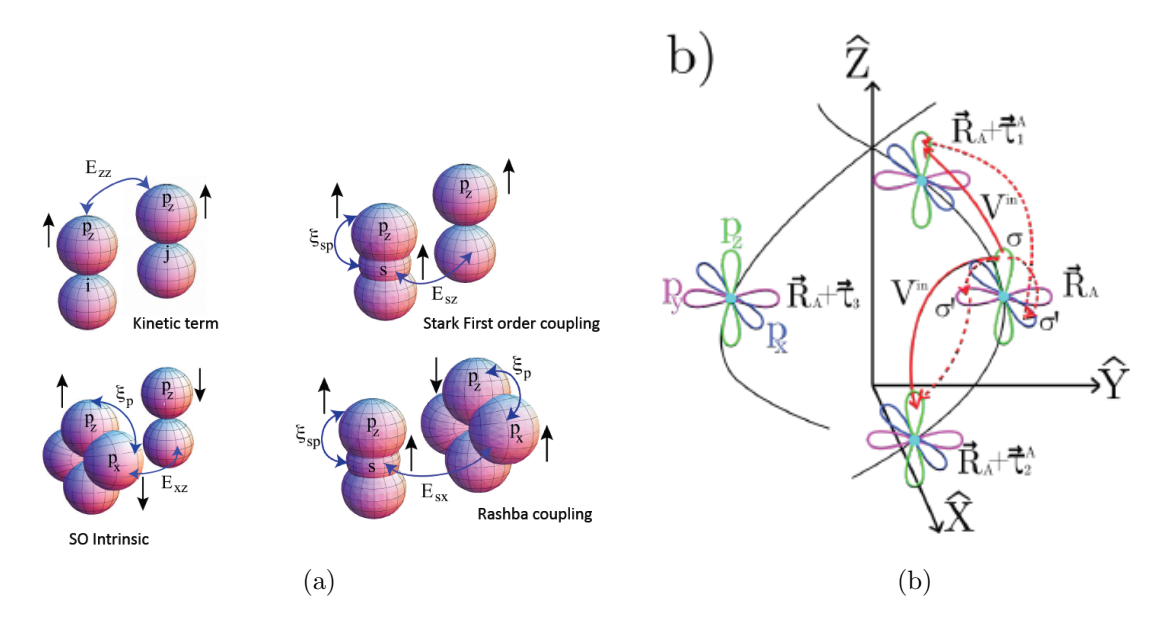


Figure 2.1: (a) Representative image of the Slater Koster terms considered for the tight-binding Hamiltonian in DNA. (b) Representation of the orbitals in a helix [49].

Several tight-binding based models have been proposed to characterize spin transport in single-stranded DNA (ssDNA) and double-stranded DNA (dsDNA) [5, 4, 3, 6]. However, these models are often limited to a site-based description, considering only one orbital with spherical symmetry per site and two degrees of freedom given by spin. In our model, each site is described by a combination of s and p orbitals, allowing the incor-

poration of hydrogen bond effects that partially polarize the molecules and create local electric fields within the system. Additionally, geometrical effects (e.g., tilt) are considered, accounting for nucleobases that are not entirely perpendicular to the axis. This level of detail modifies the final tight-binding Hamiltonian by introducing new overlap terms beyond the kinetic term.

Figure 2.1 presents the kinetic term and the higher-order hopping integrals. To calculate each of these terms, we characterized the basis vectors of the DNA unit cell and the orientation of the *p*-orbitals relative to one another. A complete set of Slater-Koster terms was obtained using the following expression:

$$E_{\mu\mu'}^{i,j} = (\hat{\mathbf{n}}(\mu_i), \hat{\mathbf{n}}(\mu'_j))V_{\mu\mu'}^{\pi} + \frac{(\mathbf{R}_{ij}, \hat{\mathbf{n}}(\mu_i))(\mathbf{R}_{ij}, \hat{\mathbf{n}}(\mu'_j))}{(\mathbf{R}_{ji}, \mathbf{R}_{ji})}(V_{\mu,\mu'}^{\sigma} - V_{\mu,\mu'}^{\pi}), \tag{2.1}$$

where  $\mu = s, p_x, p_y, p_z$  are the orbitals at sites  $\mathbf{R_i}$  and  $\mathbf{R_j}$  and let  $\hat{\mathbf{n}}(\mu_j)$  be the unitary vector in the direction of the orbital  $\mu_j$ .

The unit vectors of the s-p orbitals in the DNA helix base are given by:

$$\hat{n}_{x_i} = \cos \phi_i \hat{x} + \sin \phi_i \hat{y},$$

$$\hat{n}_{y_i} = -\sin \phi_i \hat{x} + \cos \phi_i \hat{y},$$

$$\hat{n}_{z_i} = \hat{z},$$

$$\hat{n}_{s_i} = \hat{R}_{ij},$$

where  $\phi_i$  is the angular position in cylindrical coordinates  $R_{ij}$  is the distance between i-site and j-site:

$$\mathbf{R_{ij_{intra}}} = 2a \sin \Delta \phi / 2\hat{y} + \frac{b\Delta \phi}{2\pi} \hat{z},$$
  
$$\mathbf{R_{ij_{inter}}} = 2a \cos \Delta \phi \hat{x} + 2a \sin \Delta \phi \hat{y}.$$

where  $\Delta \phi = \phi_j - \phi_i$ , a and b are the radius and the pitch of the helix, respectively.

The tilt of the helix can be described by a rotation of angle  $\theta$  around y axis:

$$R_y(\theta) = \begin{bmatrix} \cos \theta & 0 & \sin \theta \\ 0 & 1 & 0 \\ -\sin \theta & 0 & \cos \theta \end{bmatrix}.$$

The unit vectors of the orbitals are rewritten considering the tilt:

$$\hat{n}_{x_i} = \cos \theta \cos \phi_i \hat{x} + \cos \theta \sin \phi_i \hat{y} + \sin \theta \hat{z},$$

$$\hat{n}_{y_i} = -\sin \phi_i \hat{x} + \cos \phi_i \hat{y},$$

$$\hat{n}_{z_i} = \sin \theta \cos \phi_i \hat{x} + \sin \theta \sin \phi_i \hat{y} + \cos \theta \hat{z},$$

so as well the Pauli's matrices:

$$\hat{s}_{x_i} = \sigma_x \cos \theta \cos \phi_i + \sigma_y \cos \theta \sin \phi_i + \sigma_z \sin \theta, \tag{2.2}$$

$$\hat{s}_{y_i} = -\sigma_x \sin \phi_i + \sigma_y \cos \phi_i, \tag{2.3}$$

$$\hat{s}_{z_i} = \sigma_x \sin \theta \cos \phi_i + \sigma_y \sin \theta \sin \phi_i + \sigma_z \cos \theta. \tag{2.4}$$

Using Eq. 2.1 the overlaps between intra-helix and inter-helix orbitals can be calculated. The numerical values of these orbital overlaps, in meV, are:

$$V_{ss}^{\sigma(in)} = -163,$$
  $V_{pp}^{\sigma(in)} = 379,$   $V_{sp}^{\sigma(in)} = 215,$   $V_{pp}^{\pi(in)} = -94,$   $V_{sp}^{\sigma(out)} = -24,$   $V_{pp}^{\sigma(out)} = 43,$   $V_{pp}^{\pi(out)} = -10.$ 

The numerical parameters are the same of the reference [4]: a=0.7 Å, b=3.4 Å,  $\Delta\phi=2\pi/(M-1)$  where M is the number of base pairs per turn.

The complete Hamiltonian of the system has the next structure: where  $H_{\pi}$  contains the mobile electrons in the half-filled  $p_z$  orbitals of the system,  $H_{\sigma}$  encompasses all cohesive

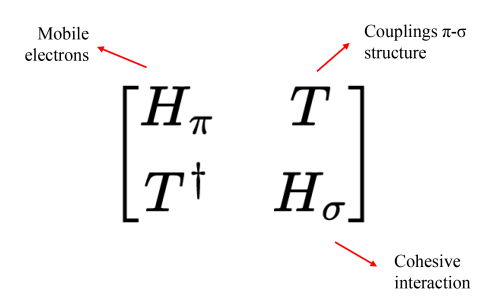


Figure 2.2: Complete Hamiltonian structure of the DNA after calculating the kinetic term, the intrinsic spin-orbit, the Stark coupling, and the Rashba coupling.

interactions in terms of the s,  $p_x$  and  $p_y$  orbitals, and T includes the terms that coupling the  $\pi$  and the  $\sigma$  interactions. The specific form of each of these sub-matrices is given by:

| $H_{\pi}$          | $ p_{zAi}\rangle$    | $ p_{zBi}\rangle$    | $ p_{zAj}\rangle$    | $ p_{zBj}\rangle$    |
|--------------------|----------------------|----------------------|----------------------|----------------------|
| $\langle p_{zAi} $ | $\epsilon^\pi_{pAi}$ | $E_{zz}^{out}$       | $E_{zz}^{in}$        | 0                    |
| $\langle p_{zBi} $ | $E_{zz}^{out}$       | $\epsilon^\pi_{pBi}$ | 0                    | $E_{zz}^{in}$        |
| $\langle p_{zAj} $ | $E_{zz}^{in}$        | 0                    | $\epsilon^\pi_{pAj}$ | $E_{zz}^{out}$       |
| $\langle p_{zBj} $ | 0                    | $E_{zz}^{in}$        | $E_{zz}^{out}$       | $\epsilon^\pi_{pBj}$ |

| $H_{\sigma}$       | $ s_{Ai}\rangle$ | $ p_{xAi} angle$       | $ p_{yAi}\rangle$     | $ s_{Bi}\rangle$ | $ p_{xBi}\rangle$      | $ p_{yBi}\rangle$     | $ s_{Aj}\rangle$ | $ p_{xAj}\rangle$      | $ p_{yAj}\rangle$     | $ s_{Bj}\rangle$ | $ p_{xBj} angle$          | $ p_{yBj}\rangle$     |
|--------------------|------------------|------------------------|-----------------------|------------------|------------------------|-----------------------|------------------|------------------------|-----------------------|------------------|---------------------------|-----------------------|
| $\langle s_{Ai} $  | $\epsilon_{sAi}$ | 0                      | $\xi_{sp}$            | 0                | 0                      | 0                     | 0                | 0                      | $V_{sp}^{in}$         | 0                | 0                         | 0                     |
| $\langle p_{xAi} $ | 0                | $\epsilon_{pxAi}$      | $i\xi_p E_{xy}^{SOC}$ | 0                | 0                      | 0                     | 0                | 0                      | 0                     | 0                | 0                         | 0                     |
| $\langle p_{yAi} $ | $\xi_{sp}$       | $-i\xi_p E_{xy}^{SOC}$ | $\epsilon_{pyAi}$     | 0                | 0                      | 0                     | $V_{ps}^{in}$    | 0                      | 0                     | 0                | 0                         | 0                     |
| $\langle s_{Bi} $  | 0                | 0                      | 0                     | $\epsilon_{sBi}$ | 0                      | $\xi_{sp}$            | 0                | 0                      | 0                     | 0                | 0                         | $V_{sp}^{in}$         |
| $\langle p_{xBi} $ | 0                | 0                      | 0                     | 0                | $\epsilon_{pxBi}$      | $i\xi_p E_{xy}^{SOC}$ | 0                | 0                      | 0                     | 0                | 0                         | 0                     |
| $\langle p_{yBi} $ | 0                | 0                      | 0                     | $\xi_{sp}$       | $-i\xi_p E_{xy}^{SOC}$ | $\epsilon_{pyBi}$     | 0                | 0                      | 0                     | $V_{ps}^{in}$    | 0                         | 0                     |
| $\langle s_{Aj} $  | 0                | 0                      | $V_{sp}^{in}$         | 0                | 0                      | 0                     | $\epsilon_{sAj}$ | 0                      | $\xi_{sp}$            | 0                | 0                         | 0                     |
| $\langle p_{xAj} $ | 0                | 0                      | 0                     | 0                | 0                      | 0                     | 0                | $\epsilon_{pxAi}$      | $i\xi_p E_{xy}^{SOC}$ | 0                | 0                         | 0                     |
| $\langle p_{yAj} $ | $V_{ps}^{in}$    | 0                      | 0                     | 0                | 0                      | 0                     | $\xi_{ps}$       | $-i\xi_p E_{xy}^{SOC}$ | $\epsilon_{pyAj}$     | 0                | 0                         | 0                     |
| $\langle s_{Bj} $  | 0                | 0                      | 0                     | 0                | 0                      | $V_{sp}^{in}$         | 0                | 0                      | 0                     | $\epsilon_{sBi}$ | 0                         | $\xi_{sp}$            |
| $\langle p_{xBj} $ | 0                | 0                      | 0                     | 0                | 0                      | 0                     | 0                | 0                      | 0                     | 0                | $\epsilon_{pxBi}$         | $i\xi_p E_{xy}^{SOC}$ |
| $\langle p_{yBj} $ | 0                | 0                      | 0                     | $V_{ps}^{in}$    | 0                      |                       | 0                | 0                      | 0                     | $\xi_{ps}$       | $-i\xi_p E_{xy}^{SOC}$    | $\epsilon_{pyBi}$     |
|                    |                  |                        |                       |                  |                        |                       |                  |                        |                       |                  |                           |                       |
| T                  | $ s_{Ai} $       | $ p_{xAi}\rangle$      | $ p_{yAi}\rangle$     | $ s_{Bi}\rangle$ | $ p_{xBi}\rangle$      | $ p_{yBi}\rangle$     | $ s_{Aj}\rangle$ | $ p_{xAj}\rangle$      | $ p_{yAj}\rangle$     | $ s_{Bj} $       | $\rangle  p_{xBj}\rangle$ | $ p_{yBj}\rangle$     |
| $\langle p_{zAi} $ | 0                | $-is_y\xi_p$           | $i\xi_p E_{zy}^{SOC}$ | $V_{zs}^{out}$   | 0                      | $E_{sz}^{in}$         | $E_{xz}^{in}$    | $E_{yz}^{in}$          | 0                     | 0                |                           |                       |
| $\langle p_{zBi} $ | $V_{zs}^{ou}$    | $E_{zx}^{out}$         | 0                     | 0                | $-is_y\xi_p$           | $i\xi_p E_{zy}^{SOC}$ | 0                | 0                      | 0                     | $E_{zs}^{in}$    | $E_{zx}^{in}$             | $E_{zy}^{in}$         |
| $\langle p_{zAj} $ | $E_{zs}^{in}$    | $E_{zx}^{in}$          | $E_{zy}^{in}$         | 0                | 0                      | 0                     | 0                | $-is_y\xi_p$           | $i\xi_p E_{zy}^{SOC}$ | $V_{zs}^{ou}$    | $E_{zx}^{out}$            | 0                     |
| $\langle p_{zBj} $ | 0                | 0                      | 0                     | $E_{zs}^{in}$    | $E_{zx}^{in}$          | $E_{zy}^{in}$         | $V_{zs}^{out}$   | $E_{zx}^{out}$         | 0                     | 0                | $-is_y\xi_p$              | $i\xi_p E_{zy}^{SOC}$ |

here the diagonal terms  $(\epsilon_{i,j})$  are the HOMO-LUMO energies of each nucleobase of the DNA: These values are calculated using tight-binding methods and compared with those

| Energy [eV] | Adenine | Thymine | Cytosine | Guanine |
|-------------|---------|---------|----------|---------|
| $E_{HOMO}$  | -8.2    | -9.0    | -8.2     | -8.9    |
| $E_{LUMO}$  | -4.4    | -4.8    | -4.4     | -4.4    |

Table 2.1: Orbital energies of DNA base pairs calculated through tight-binding methods, as reported in ref. [8].

obtained through other approaches in ref. [8]. Only homogeneous combinations of nucleobases are considered; i.e., the ssDNA is composed of adenine bases, with diagonal energies set to their HOMO levels. Additionally, the dsDNA consists solely of A-T pairs, where the adenine strand has the HOMO energy, while the thymine strand has the LUMO energy of thymine. This aspect, often overlooked in previous works, is significant because it has been demonstrated that site energy disorder impacts electronic transmission [50, 51, 6].

#### 2.2 Slater-Koster Terms

#### The Kinetic Term

The lowest order term comes from the overlapping between the  $p_z$  orbitals in the system. It depends on the geometrical parameters described in the latter section

$$H_K^{in} = \sum_{i,j} E_{zz}^{in} c_i^{\dagger} c_j, \qquad (2.5)$$

$$\begin{split} E_{zz}^{in} &= (\sin^2\theta\cos\Delta\phi + \cos^2\theta)V_{pp}^{\pi(in)} + \left[\frac{b\Delta\phi\cos\theta}{2\pi} - 2a\sin(\Delta\phi/2)\sin\theta\sin\phi_i\right] \\ &\left[\frac{b\Delta\phi\cos\theta}{2\pi} - 2a\sin(\Delta\phi/2)\sin\theta\sin\phi_j\right] \left[\frac{V_{pp}^{\sigma(in)} - V_{pp}^{\pi(in)}}{|\mathbf{R_{ij_{intra}}}|^2}\right], \end{split}$$

where i and j are the i-site and the j-site in the same helix (A-A and B-B). On the other hand, the kinetic term outside the helix depends only on the tilt:

$$H_K^{out} = E_{zz}^{out} \sum_{i,j} c_i^{\dagger} c_j, \tag{2.6}$$

$$E_{zz}^{out} = \cos^2 \theta V_{pp}^{\pi} - \sin^2 \theta V_{pp}^{\sigma}$$

where i and j are the i-site in the helix A and the j-site in the helix B.

#### The Stark Effect

The transition between the  $p_z$  orbitals of different sites is also possible due to the sp coupling. This effect is the consequence of the electric fields in the chiral structure of the DNA, as it has been pointed.

$$\langle s|H_S|p_z\rangle = 2ea_0E_Z = \xi_{sp} \tag{2.7}$$

where the Slater-Koster term follows the expression:

$$E_{sz}^{in} = \left[ -2a\sin(\Delta\phi/2)\sin\theta\sin\phi_i + \frac{b\Delta\phi}{2\pi}\cos\theta \right] \frac{V_{sp}^{\sigma(in)}}{|\mathbf{R_{iiintra}}|}$$

The geometry of the orbitals enables the Stark coupling between strands:

$$E_{sz}^{out} = -\sin\theta V_{sp}^{\sigma(out)}$$

#### The Intrinsic SO Effect

The intrinsic spin-orbit coupling in carbon atoms provides a spin-active pathway for electrons. The overlap between the  $p_z$  and the  $p_x$ ,  $p_y$  orbitals at the same site enables spin flipping, allowing the electron to subsequently hop to the  $p_z$  orbital at another site. It is worth mentioning that models such as the Guo and Sun model introduce SOC as coupling

between the i-site and i+1-site. In contrast, in the proposed model, SOC arises naturally from including higher-order interactions within the atomic orbitals.

$$H_{SO} = \frac{e\hbar}{4m_0^2 c^2} \mathbf{s} \cdot (\mathbf{p} \times \nabla V)$$
 (2.8)

$$= -\frac{1}{r} \frac{\partial V}{\partial r} \frac{e\hbar}{2m_0^2 c^2} \mathbf{L} \cdot \mathbf{s}$$
 (2.9)

$$= \lambda \mathbf{L} \cdot \mathbf{s} \tag{2.10}$$

All the possible matrix elements are summarized in the table:

|                 | $ p_x angle$       | $ p_y\rangle$        | $ p_z\rangle$      |
|-----------------|--------------------|----------------------|--------------------|
| $\langle p_x  $ | 0                  | -i $\hat{s}_z \xi_p$ | $i\hat{s}_y\xi_p$  |
| $\langle p_y $  | $i\hat{s}_z\xi_p$  | 0                    | $-i\hat{s}_x\xi_p$ |
| $\langle p_z $  | $-i\hat{s}_y\xi_p$ | $i\hat{s}_x\xi_p$    | 0                  |

where  $\xi_p = \lambda \hbar/2$  is the spin-orbit strength that was set in a numerical value of 6 meV for the simulations and  $\hat{s}_i$  are the Pauli's matrices in the helix base described in Eq. 2.4. The Slater-Koster terms of the coupling between the  $p_z$  and the  $p_x$ ,  $p_y$  orbitals are given by:

$$E_{xz}^{in} = -\cos\theta \sin\theta (\cos(\Delta\phi) - 1)V_{pp}^{\pi(in)} + \left[ 2a\sin(\Delta\phi/2)\cos\theta \sin\phi_i + \frac{b\Delta\phi}{2\pi}\sin\theta \right]$$
$$\left[ -2a\sin(\Delta\phi/2)\cos\theta \sin\phi_j + \frac{b\Delta\phi}{2\pi}\cos\theta \right] \left[ \frac{V_{pp}^{\sigma(in)} - V_{pp}^{\pi(in)}}{|\mathbf{R}_{ij_{intra}}|^2} \right]$$

$$E_{yz}^{in} = \sin\theta \sin(\Delta\phi) V_{pp}^{\pi(in)} + 2a \sin(\Delta\phi/2) \cos\phi_i$$

$$\left[ \frac{b\Delta\phi}{2\pi} \cos\theta - 2a \sin(\Delta\phi/2) \sin\theta \sin\phi_j \right] \left[ \frac{V_{pp}^{\sigma(in)} - V_{pp}^{\pi(in)}}{|\mathbf{R}_{\mathbf{ij_{intra}}}|^2} \right]$$

Similarly to the Stark effect, the Slater-Koster terms outside the helix can be calculated using the specific orbital geometry:

$$E_{xz}^{out} = \cos\theta \sin\theta (V_{pp}^{\pi(out)} - V_{pp}^{\sigma(out)})$$
  
$$E_{yz}^{out} = 0$$

#### Rashba Interaction

Combining the Stark effect and the intrinsic spin-orbit coupling gives rise to the Rashba effect. This term enables overlap between the s orbital of a site and the px, py orbitals of another site:

$$E_{sx}^{in} = \left(2a\sin(\Delta\phi/2)\sin\phi_i\cos\theta + \frac{b\Delta\phi}{2\pi}\sin\theta\right) \frac{V_{sp}^{\sigma(in)}}{|\mathbf{R}_{i\mathbf{j_{intra}}}|}$$

$$E_{sy}^{in} = \frac{2a\sin(\Delta\phi/2)\cos\phi_i}{|\mathbf{R}_{i\mathbf{j_{intra}}}|}V_{sp}^{\sigma(in)}$$

$$E_{sx}^{out} = \cos\theta V_{sp}^{\sigma(out)}$$

$$E_{sy}^{out} = 0$$

The other Slater-Koster terms were calculated

$$E_{ss}^{in} = V_{ss}^{in} \,$$

$$\begin{split} E_{xx}^{in} &= [\cos\theta^2\cos(\Delta\phi) + \sin\theta^2] V_{pp}^{\pi(in)} + (4a^2\sin^2(\Delta\phi/2)\sin\phi_i\sin\phi_j + \\ &+ 2a\sin(\Delta\phi/2)b\Delta\sin\theta\cos\theta(\sin\phi_i + \sin\phi_j) / 2\pi + \frac{b^2(\Delta\phi)^2\sin^2\theta}{4\pi^2}) \left[ \frac{V_{pp}^{\sigma(in)} - V_{pp}^{\pi(in)}}{|\mathbf{R_{ij_{intra}}}|^2} \right], \end{split}$$

$$\begin{split} E_{xy}^{in} &= \cos\theta \sin(\Delta\phi) V_{pp}^{\pi(in)} + 2a \sin(\Delta\phi/2) \cos\phi_j \\ & \left[ 2a \sin(\Delta\phi/2) \cos\theta \sin\phi_i + \frac{b\Delta\phi}{2\pi} \sin\theta \right] \left[ \frac{V_{pp}^{\sigma(in)} - V_{pp}^{\pi(in)}}{|\mathbf{R_{ij_{intra}}}|^2} \right], \end{split}$$

$$E_{yy}^{in} = \cos \Delta \phi V_{pp}^{\pi(in)} + 4a^2 \sin^2(\Delta \phi/2) \cos \phi_i \cos \phi_j \left[ \frac{V_{pp}^{\sigma(in)} - V_{pp}^{\pi(in)}}{|\mathbf{R_{ij_{intra}}}|^2} \right],$$

$$\begin{split} E_{ss}^{out} &= V_{ss}^{\sigma(out)}, \\ E_{xx}^{out} &= \sin^2 \theta V_{pp}^{\pi(out)} - \cos^2 \theta V_{pp}^{\sigma(out)}, \\ E_{yy}^{out} &= 0, \\ E_{xy}^{out} &= 0. \end{split}$$

#### 2.3 Landauer Formalism

To perform transport measurements, two electrodes are connected to both ends of the molecule, with both leads modeled as perfect semi-infinite 1D chains. To illustrate the effects of the leads on the site energies of the system, we refer to the calculations presented by Pastawski and Medina [52]. Consider the Hamiltonian shown in Figure 2.2 in its decimated form.

$$\mathcal{H}_{0} = E_{1} |p_{z1}\rangle \langle p_{z1}| + E_{N} |p_{zN}\rangle \langle p_{zN}| + V_{1,N} |p_{z1}\rangle \langle p_{zN}| + V_{N,1} |p_{zN}\rangle \langle p_{z1}|, \qquad (2.11)$$

where E and V are functions of the variable  $\epsilon$  and  $p_{z1}$  ( $p_{zN}$ ) are the  $p_z$  orbitals of the first (last) site in the strand. The dispersion relations of the electrodes are:

$$E_{kL,(R)} = E_{L,(R)} + 2V_{L,(R)}\cos(k_{L,(R)}a), \qquad (2.12)$$

L(R) refers to the left (right) lead.

The system connected to the leads can be described in terms of the  $p_z$  orbitals and

the couplings between the leads and system  $V_{tL(tR)}$ 

$$\mathcal{H}_{0-leads} = V_{tL}(|p_{z1}\rangle \langle p_{z0}| + |p_{z0}\rangle \langle p_{z1}|) + V_{tR}(|p_{zN}\rangle \langle p_{zN+1}| + |p_{zN+1}\rangle \langle p_{zN}|)$$
(2.13)

The site energies where the leads are connected include the self-energy produced by the leads:

$${}^{L}\Sigma_{1} = \left|\frac{V_{tL}}{V_{L}}\right|^{2} (|V_{L}|\cos(k_{L}a) - i|V_{L}|\sin(k_{L}a))$$
(2.14)

$$=^{L} \Delta_1 - i^L \Gamma_1, \tag{2.15}$$

$${}^{R}\Sigma_{1} = \left| \frac{V_{tR}}{V_{R}} \right|^{2} (|V_{R}| \cos(k_{R}a) - i|V_{R}| \sin(k_{R}a))$$
 (2.16)

$$=^{R} \Delta_{N} - i^{R} \Gamma_{N}. \tag{2.17}$$

These expressions can be calculated in terms of the energy following the decimation procedure described in [52]:

$$\Sigma^{R}(\epsilon) = \left| \frac{V_{R}}{V_{0}} \right|^{2} \left[ \frac{(\epsilon - E_{0})}{2} - i\sqrt{4V_{0}^{2} - (\epsilon - E_{0})^{2}}/2 \right]$$
 (2.18)

The leads produce an effective potential of the form:

$$\hat{\mathcal{H}}_{eff} = \hat{\mathcal{H}}_0 + {}^{L} \Sigma_1 |p_{z0}\rangle \langle p_{z0}| + {}^{R} \Sigma_N |p_{zN+1}\rangle \langle p_{zN+1}|.$$
 (2.19)

Note that the leads are described solely in terms of their  $p_z$  orbitals, without additional orbital interactions or spin-active properties. Depolarized electrons are injected from the  $p_z$  orbital of the lead to the  $p_z$  orbital of the system. Finally, the Green's function can be obtained from the effective Hamiltonian:

$$G^{R,(A)}(\epsilon) = [(\epsilon \pm i\eta)\hat{\mathcal{I}} - \hat{\mathcal{H}}_{eff}]^{-1}.$$
 (2.20)

Additionally, the gray region in Fig. 2.3 indicates that the density of states (DoS) of the

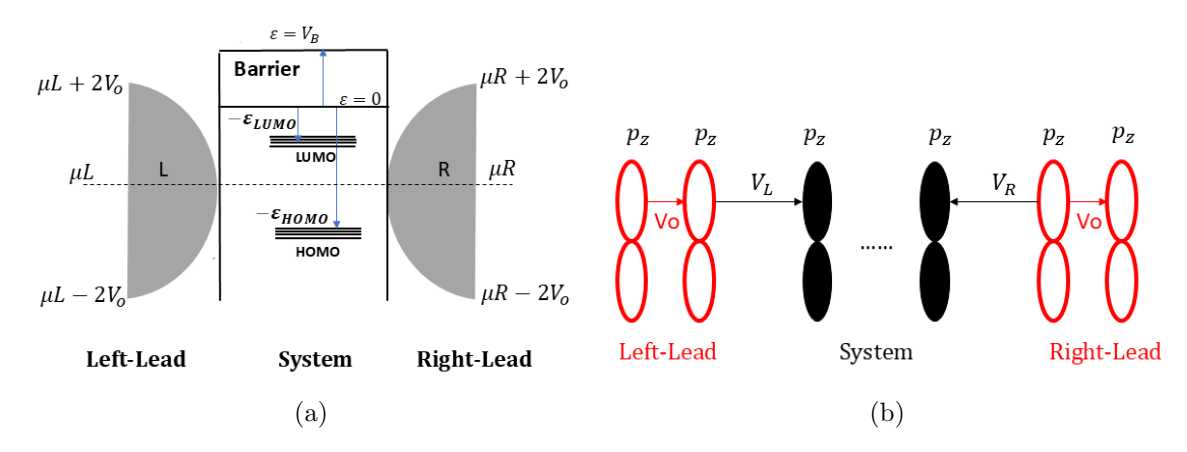


Figure 2.3: Schematic representation of the molecule's energy levels when connected to leads. Here,  $\mu_R$  and  $\mu_L$  denote the chemical potentials of the right and left leads, respectively;  $V_0$  is the coupling within the lead sites, and  $V_R$  and  $V_L$  are the right and left couplings between the system and the leads. a) Energy diagram with the vertical axis representing energy levels and the horizontal axis showing the position of the leads and the system. b) Schematic of orbital connections between the leads and the system.

leads follows the semi-circle law, allowing transmission only when the injection energy falls within the interval  $[\mu_{R,L} - 2V_0, \mu_{R,L} + 2V_0]$ . The expression for such a density of state can be calculated from the Green's function:

$$N_i(\epsilon) = \frac{1}{\pi} \lim_{\eta \to 0} \operatorname{Im} G_{ii}^R(\epsilon + i\eta). \tag{2.21}$$

Given that the leads are semi-infinite chains connected to the system, the Green's function at the surface site is:

$$G_{1,1}^{R} = \frac{1}{\epsilon - E_0 - \Sigma^R(\epsilon)},$$
 (2.22)

replacing the expression for  $\Sigma^R(\epsilon)$  and comparing with eq. 2.21, the semi-circle law is obtained:

$$N_1(\epsilon) = \frac{1}{\pi V_0} \sqrt{1 - \left(\frac{\epsilon - E_0}{2V_0}\right)^2}.$$
 (2.23)

Using the Fisher-Lee formula [53], we obtain the transmission between the leads in terms of the self energies of the leads and the retarded  $\mathbf{R}$  and advanced  $\mathbf{A}$  Green's functions:

$$T_{\alpha R,\beta L} = [2^{\alpha} \Gamma_R(\epsilon)] G_{\alpha R,\beta L(\epsilon)}^{\mathbf{R}} [2^{\beta} \Gamma_L(\epsilon)] G_{\alpha L,\beta R(\epsilon)}^{\mathbf{A}}.$$
 (2.24)

The  $\alpha$ ,  $\beta$  indicated the process or channel associated with the electron decay. The

conductance can be expressed as:

$$\mathcal{G}_{R,L} = 4 \frac{e^2}{h} Tr[\Gamma_R(\epsilon) G_{R,L(\epsilon)}^{\mathbf{R}} \Gamma_L(\epsilon) G_{L,R}^{\mathbf{A}}(\epsilon)]. \tag{2.25}$$

In CISS research, "spin polarization" is commonly defined as the difference between measurable quantities associated with a spin-selective process divided by their sum. For instance, polarization in the CISS literature is often represented as normalized anisotropies in electron currents or charge transfer rate constants, which can be influenced by the spin density of states [9]. The spin polarization  $(P_s)$  in all the presented results is derived in terms of the conductances from Eq. 2.37:

$$P_s = \frac{\mathcal{G}_{\uparrow} - \mathcal{G}_{\downarrow}}{\mathcal{G}_{\uparrow} + \mathcal{G}_{\downarrow}}.\tag{2.26}$$

### 2.4 Dephasing

During the transport process, the electron experiences a loss of phase memory due to inelastic interactions (e.g., electron-phonon interaction, inelastic impurity scattering, electronelectron interaction, etc.). To simulate these considerations, a third probe must be introduced into the system. There is expected no spin polarization in a fully phase-coherent two-terminal conduction, the time-reversal symmetry is preserved, as it is stated in the reciprocity relations. Assuming the application of these rules for any conductor, the reciprocity theorem states that, for a multi-terminal circuit in the linear regime, the conductance measurement is invariant under the exchange of voltage and current when both the magnetization (M) and the magnetic field (H) are inverted:

$$\mathcal{G}_{ij}(H,M) = \mathcal{G}_{ij}(-H,-M). \tag{2.27}$$

This theorem is valid for any linear-regime circuit, regardless of the number of terminals or the microscopic dephasing process [54].

Applying the reciprocity theorem to chiral molecules provides insight into the trans-

mission properties of CISS. Particularly, in a two-terminal system, the theorem requires that the conductance remains unchanged under the reversion of the ferromagnetic magnetization. Given that the conductance is related to the transmission probability, it follows that:

$$T_{ij}(\Rightarrow) = T_{ij}(\Leftarrow),$$
 (2.28)

where the direction of the arrows indicates the direction of the magnetization.

In terms of the spin, it is possible to write the transmission and reflection of the electrons propagated in the right direction in their matrix form:

$$T = \begin{bmatrix} t_{\to \to} & t_{\leftarrow \to} \\ t_{\to \leftarrow} & t_{\leftarrow \leftarrow} \end{bmatrix} R = \begin{bmatrix} r_{\to \to} & r_{\leftarrow \to} \\ r_{\to \leftarrow} & r_{\leftarrow \leftarrow} \end{bmatrix}$$
 (2.29)

For the left moving electrons, the above matrices are time-reversed:

$$T = \begin{bmatrix} t_{\leftarrow\leftarrow} & t_{\rightarrow\leftarrow} \\ t_{\leftarrow\rightarrow} & t_{\rightarrow\rightarrow} \end{bmatrix} R = \begin{bmatrix} r_{\leftarrow\leftarrow} & r_{\rightarrow\leftarrow} \\ r_{\leftarrow\rightarrow} & r_{\rightarrow\rightarrow} \end{bmatrix}$$
 (2.30)

These terms connect the quantum description with a macroscopic approach in experiments. It is possible to write this conductance in a matrix equation for the total current I and the spin current  $I_s$ :

$$\begin{bmatrix} I \\ -I_{sL} \end{bmatrix} = -\frac{Ne}{h} \begin{bmatrix} t & P_t t \\ P_t t & \gamma_r \end{bmatrix} \begin{bmatrix} \mu_L - \mu_R \\ \mu_{sL} \end{bmatrix}$$
 (2.31)

Where  $\mu_L$  and  $\mu_R$  are the chemical potential of the leads and  $\mu_{sL} = (\mu_{\to} - \mu_{\leftarrow})/2$ . This matrix equation fully describes the coupled charge and collinear spin transport through a (nonmagnetic) chiral component, which is subject to Onsager's reciprocity in the linear

response regime, where the following relations are fulfilled

$$t = t_{\to \to} + t_{\to \leftarrow} + t_{\leftarrow \to} + t_{\leftarrow \leftarrow}, \tag{2.32}$$

$$r = r_{\to\to} + r_{\to\leftarrow} + r_{\leftarrow\to} + r_{\leftarrow\leftarrow} = 2 - t, \tag{2.33}$$

$$\gamma_t = t_{\to \to} - t_{\to \leftarrow} - t_{\leftarrow \to} + t_{\leftarrow \leftarrow}, \tag{2.34}$$

$$\gamma_r = r_{\to\to} - r_{\to\leftarrow} - r_{\leftarrow\to} + r_{\leftarrow\leftarrow}, \tag{2.35}$$

$$P_t = (t_{\to \to} - t_{\to \leftarrow} + t_{\leftarrow \to} - t_{\leftarrow \leftarrow})/t, \tag{2.36}$$

$$P_r = (r_{\to \to} - r_{\to \leftarrow} + r_{\leftarrow \to} - r_{\leftarrow \leftarrow})/r, \tag{2.37}$$

$$s = t_{\to \to} + t_{\to \leftarrow} - t_{\leftarrow \to} - t_{\leftarrow \leftarrow}, \tag{2.38}$$

$$= -r_{\to\to} - r_{\to\leftarrow} + r_{\leftarrow\to} + r_{\leftarrow\leftarrow}. \tag{2.39}$$

For a more detailed description of the macroscopic approach and the Onsager reciprocity breaking in a ferromagnetic/chiral element, see reference [55].

The third probe introduced in the model acts as a probability leakage, leading to a loss of unitarity in the transmission. Electrons exiting the sample toward this lead are entirely incoherent with those entering. However, more sophisticated models, such as the D'Amato-Pastawski model, preserve unitarity by imposing a voltmeter probe condition on the lead. Like the two-terminal leads, this probe is characterized by its self-energy.

$$^{\phi}\Sigma_{i} = -i^{\phi}\Gamma_{d}. \tag{2.40}$$

It is possible to define a dephasing length in terms of the imaginary part of the self-energy  ${}^{\phi}\Gamma_d$ :

$$\frac{2\Gamma_d}{\hbar} = \frac{1}{\tau_\phi},\tag{2.41}$$

where  $\tau_{\phi}$  is the dephasing time. Let us call x the direction of electron injection, a charac-

teristic length can be associated with  $\tau_{\phi}$ :

$$L_{\phi} = \frac{p_x \tau_{\phi}}{m},\tag{2.42}$$

$$=\frac{p_x\hbar}{2m\Gamma_d},\tag{2.43}$$

$$= \frac{p_x \hbar}{2m\Gamma_d},$$

$$= \frac{k_x \hbar^2}{2m\Gamma_d},$$
(2.43)

where  $k_x$  is the wave vector associated with the energy injection.

Eq. 2.44 indicates the dephasing that the electron suffers caused by the decoherent event. It is easy to see that when  $\Gamma_d \to 0$ , then  $L_\phi \to \infty$  is consistent with the statement that there is no spin polarization without decoherence.

Given that leads are the main source of decoherence, the Landauer formalism is useful in characterizing the transmission in the three-probe system. The procedure resulting from applying Kirchhoff's law to each lead is called the Landauer-Büttiker equation.

$$\tilde{T}_{R,L} = T_{R,L} + \frac{T_{R,\phi}T_{\phi,L}}{T_{R,\phi} + T_{\phi,L}},$$
(2.45)

where the first term is identified as the coherent transmission, while the second is the incoherent contribution to the current. The Eq. 2.45 can be expressed in terms of the conductances:

$$\tilde{\mathcal{G}}_{R,L} = \mathcal{G}_{R,L} + (\mathcal{G}_{R,\phi}^{-1} + \mathcal{G}_{\phi,L}^{-1})^{-1},$$
(2.46)

which can be identified as the equivalent inverse of resistance in a circuit.

The transmission of Eq. 2.44 can be extended to various decoherent probes in different sites of the molecule:

$$\tilde{T}_{R,L} = T_{R,L} + \sum_{j=1}^{N} \sum_{i=1}^{N} T_{R,j} [\mathbf{W}^{-1}]_{j,i} T_{i,L},$$
(2.47)

where

$$\mathbf{W} = \begin{bmatrix} T_{1,1} - 1/g_1 & T_{1,2} & T_{1,3} & \dots & T_{1,N} \\ T_{2,1} & T_{2,2} - 1/g_2 & T_{2,3} & \dots & T_{2,N} \\ T_{3,1} & T_{3,2} & T_{3,3} - 1/g_3 & \dots & T_{3,N} \\ \vdots & \vdots & \ddots & \vdots & \vdots \\ T_{N,1} & T_{N,2} & T_{N,3} & \dots & T_{N,N} - 1/g_N \end{bmatrix}$$

where  $g_i$  are the adimensional conductances of each site, i.e., they are just the transmission probabilities that can be calculated from Eq. 2.24.

#### 2.5 Band Folding

Considering the total Hamiltonian described in the first section, where each site has four orbitals with two spin degrees of freedom, it is challenging to perform a qualitative analysis of the molecule's transport properties. Obtaining an analytical description of the model is useful for better understanding spin behavior during transport. Therefore, it is convenient to implement an effective Hamiltonian in the  $p_z$  orbital space, with the  $\sigma$ -structure interaction introduced perturbatively.

The Foldy-Wouthuysen transformation is a unitary transformation of the orthonormal basis in which both the Hamiltonian and the wave function are represented [56]. The eigenvalues remain unchanged under such a unitary transformation, indicating that the physics is unaffected by this change in the unitary basis. Consequently, such a unitary transformation can always be applied; specifically, one can choose a unitary basis transformation that reformulates the Hamiltonian into a more convenient form. Consider the Hamiltonian of Fig. 2.2, the effective Hamiltonian where the space  $\pi$  is  $4 \times 4$ , and the  $\sigma$  space is  $12 \times 12$  with two degrees of freedom for the spin both. Let us call the eigenfunction of the complete Hamiltonian  $\psi = (\psi_{\pi}, \psi_{\sigma})^T$  where it can be written in the form:

$$\begin{bmatrix} H_{\pi} & T \\ T^{\dagger} & H_{\sigma} \end{bmatrix} \begin{bmatrix} \psi_{\pi} \\ \psi_{\sigma} \end{bmatrix} = E \begin{bmatrix} \psi_{\pi} \\ \psi_{\sigma} \end{bmatrix}$$
 (2.48)

where it is possible to write the  $\sigma$  component of the eigenfunction in terms of the  $\pi$  component:

$$\psi_{\sigma} = (E - H_{\sigma})^{-1} T^{\dagger} \psi_{\pi}, \tag{2.49}$$

Substituting this into the first row of 2.48 gives an effective eigenvalue equation written solely for the  $\pi$  components:

$$[H_{\pi} - T(E - H_{\sigma})^{-1}T^{\dagger}]\psi_{\pi} = E\psi_{\pi}, \tag{2.50}$$

$$[H_{\pi} - TH_{\sigma}^{-1}T^{\dagger}]\psi_{\pi} \approx E\mathcal{S}\psi_{\pi}, \tag{2.51}$$

where  $S = \hat{I} + T H_{\sigma}^{-2} T^{\dagger}$ . Finally, the transformation  $\Phi = S^{1/2} \psi_{\pi}$  is performed:

$$[H_{\pi} - TH_{\sigma}^{-1}T^{\dagger}]\mathcal{S}^{-1/2}\Phi = E\mathcal{S}^{1/2}\Phi, \tag{2.52}$$

$$S^{-1/2}[H_{\pi} - TH_{\sigma}^{-1}T^{\dagger}]S^{-1/2}\Phi = E\Phi, \qquad (2.53)$$

where the final effective Hamiltonian is:

$$H_{eff} \approx \mathcal{S}^{-1/2} [H_{\pi} - T H_{\sigma}^{-1} T^{\dagger}] \mathcal{S}^{-1/2}.$$
 (2.54)

This transformation ensures the normalization of the new eigenfunction in the  $\pi$ -space being consistent with the normalization of the original eigenstate:

$$\Phi^{\dagger}\Phi = \psi_{\pi} \mathcal{S}\psi_{\pi}, \tag{2.55}$$

$$= \psi_{\pi}^{\dagger} (\hat{I} + T H_{\sigma}^{-2} T^{\dagger}) \psi_{\pi}, \tag{2.56}$$

$$\approx \psi_{\pi}^{\dagger} \psi_{\pi} + \psi_{\sigma}^{\dagger} \psi_{\sigma}. \tag{2.57}$$

# Chapter 3

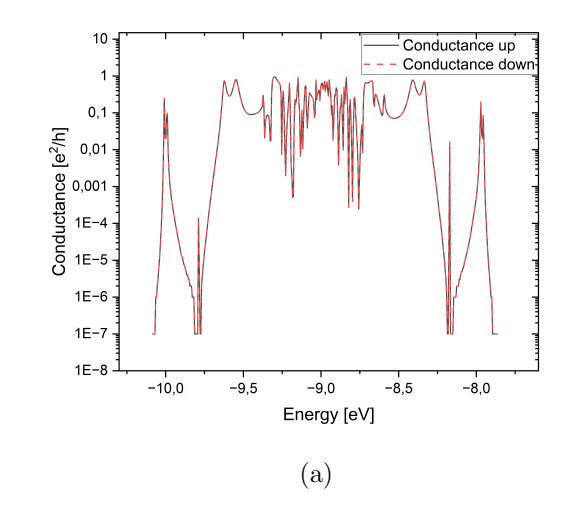
## Results

The conductances and the spin polarization as a function of the injection energy are characterized in the ssDNA and dsDNA. A qualitative analysis of spin transport behavior in the ssDNA and dsDNA, under varying parameters, is presented in terms of the averaged spin polarization where the  $\langle P_s \rangle$  is averaged in the interval  $[E_{HOMO} - k_B T, E_{HOMO} + k_B T]$ . Notably, these values represent averages over specific energy ranges and appear small due to the narrow width of the peaks. When the spin polarization is computed as a function of the injection energy, as shown in Figure 3.1 (b) Peaks can reach up to 80 % with increased dephasing coupling in both analyzed cases. The non-monotone nature of spin polarization and conductance, while not commonly observed in experiments, could result from the disorder in the energies of the system that takes to resonant peaks at different injection energies.

#### 3.1 Spin Polarization in ssDNA

To characterize the electron transport in the ssDNA, a chain of N=30 sites was simulated. The coupling of the electrodes to the system is set to  $V_{tR}=V_{tL}=1~eV$ , and the coupling to the dephasing probe is weak  $\Gamma_d=0.06~eV$  to approximate the third probe to a virtual probe.

Figure 3.1 (a) shows the conductance of spin up and the conductance of spin down in terms of the electron energy around the lead's chemical potential,  $\mu = -9 \ eV$ , which



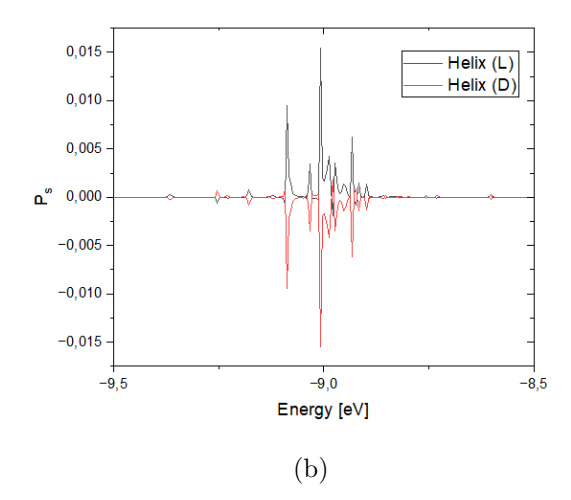
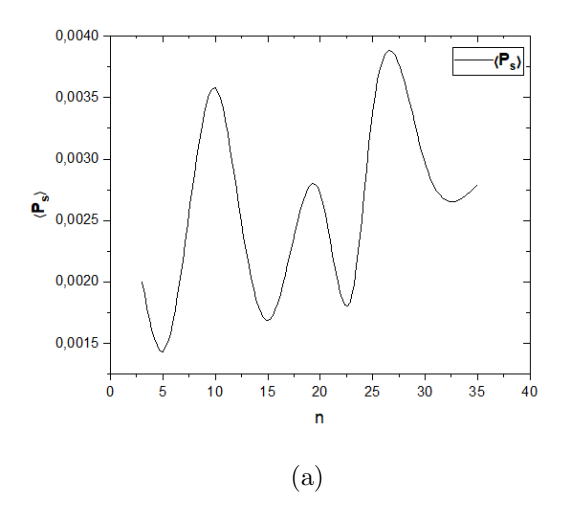


Figure 3.1: Conductances in terms of the spin and spin polarization in ssDNA. (a) Spin conductance on a logarithmic scale as a function of electron injection energy in ssDNA. (b) Spin polarization of ssDNA as a function of electron injection energy, with inverted chirality: L-left-handed (black) and D-right-handed (red).

is close to the HOMO energy levels of the system. Differences between  $\mathcal{G}_{\uparrow}$  and  $\mathcal{G}_{\downarrow}$  are observable on the order of  $10^{-2}$ . More evident differences can be obtained by adjusting parameters such as the coupling strength of the decoherence probe to the system  $(\Gamma_d)$  or by connecting additional dephasing probes. The observed spin polarization shows values around 1.5%, contrasting with the results in ref. [4], where no spin polarization was reported, and in the ref. [5], which incorporated interactions with additional nearest neighbors and reported a spin polarization of around  $\sim 10^{-5}$  in ssDNA.

Notably, the spin relaxation length is generally longer than the physical length of the molecule, so spin polarization should persist even as the molecule's length increases, as shown in Figure 3.2 (a). This increase is not monotonic but follows an interference pattern resulting from temperature effects, consistent with experimental observations reported in ref. [57].

Figure 3.2 (b) shows spin polarization as a function of the coupling strength of the dephasing probe to the system. Note that when the coupling  $\Gamma_d = 0$ , there is no spin polarization in the system as it is expected given the reciprocity relations. As  $\Gamma_d$  increases, spin polarization also rises to values around  $\langle P_s \rangle = 14\%$ . However, beyond a certain threshold, spin polarization starts to decrease as inelastic scattering events dis-



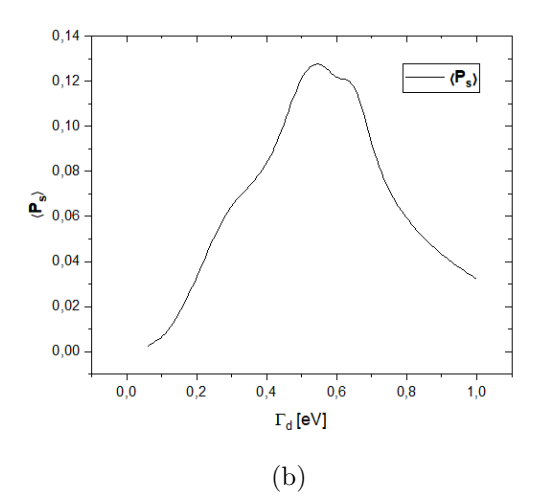


Figure 3.2: Average spin polarization in ssDNA as a function of a) number of turns (n) b) the coupling strength of the dephasing probe to the system.

rupt spin transmission between the leads. This behavior has also been reported in [5], where decoherence effects are introduced in a similar manner.

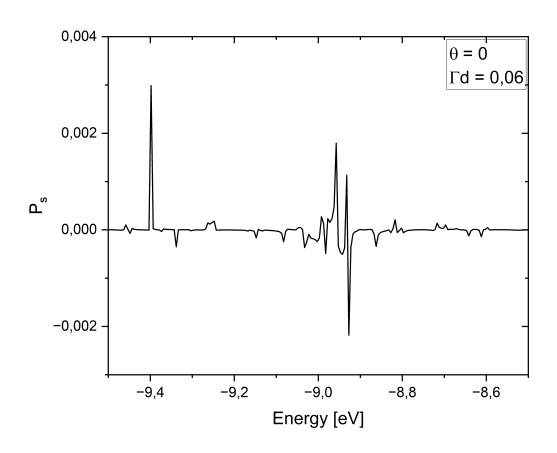


Figure 3.3: Spin polarization in ssDNA as a function of the injection energy with the decoupling strength  $\Gamma_d = 0.06$  without tilt  $(\theta = 0)$ .

Figure 3.3 shows the effect of the absence of tilt on the spin polarization. When the tilt is removed, spin polarization decreases by approximately an order of magnitude compared to the values in Figure 3.1 (b). This reduction occurs because tilt is crucial in orbital overlap, facilitating additional electron transport channels that enhance spin filtering. Nevertheless, the intrinsic helicity of the molecule preserves a degree of spin polarization. This suggests that even without tilt, the chiral structure of the helix provides

a foundational spin-selective pathway, though at a lower efficiency.

#### 3.1.1 Tunneling effect

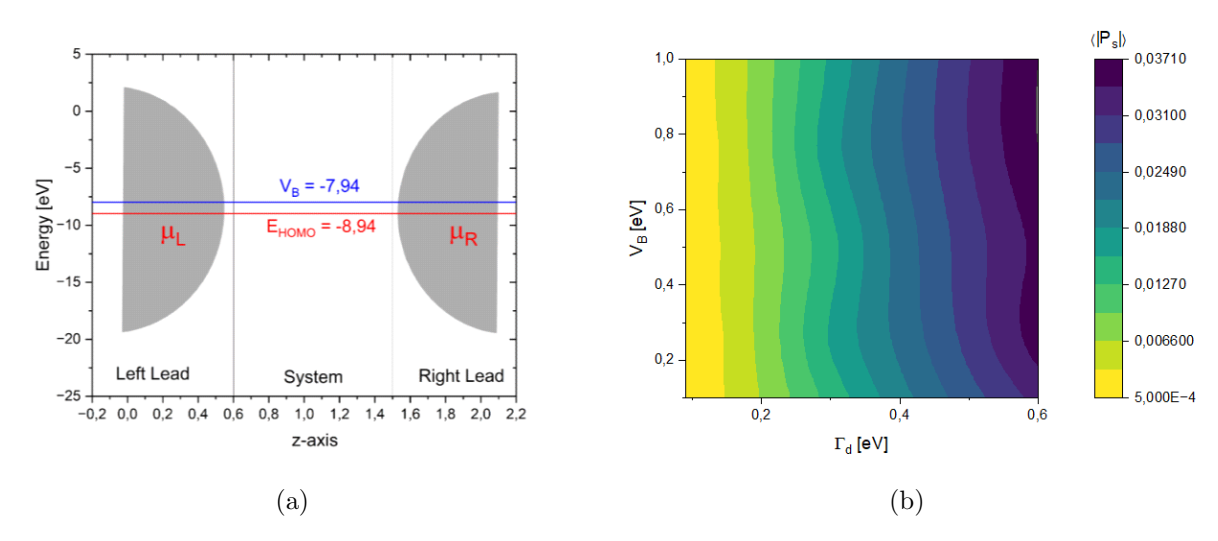


Figure 3.4: (a) Energy scheme of the injection energies in the leads, the energy of the system and the barrier intensity. (b) Average spin polarization in ssDNA as a function of the barrier intensity  $(V_B)$  and the dephasing coupling strength  $(\Gamma_d)$ .

As previously discussed, the tunneling effect is crucial in analyzing electron behavior within the molecule. The barrier was simulated by applying an external potential to the system's energy sites, causing an initial drop in conductance since the electron transmission probability is inversely proportional to the barrier height. However, spin polarization is expected to increase. Figure 3.4 illustrates how average spin polarization rises as the barrier intensity  $(V_B)$  increases. This behavior is not strictly monotonic; instead, it exhibits an interference pattern similar to the one observed when spin polarization is evaluated as a function of the number of turns (see Figure 3.2 (a)).

Figure 3.5 illustrates the impact of adding a barrier to the system on spin polarization. As expected, spin polarization increases with rising SOC strength and dephasing coupling strength. However, it is important to note that the spin-orbit coupling (SOC) considered here corresponds to the intrinsic atomic SOC, which is inherently small and varies on the order of meV. Alternatively, to other works that insert SOC as a variable parameter, spin polarization in the system can be enhanced by minimizing the SOC and instead varying parameters such as the barrier intensity and the dephasing coupling strength. This

approach demonstrates that external factors can be crucial in amplifying spin-selective effects.

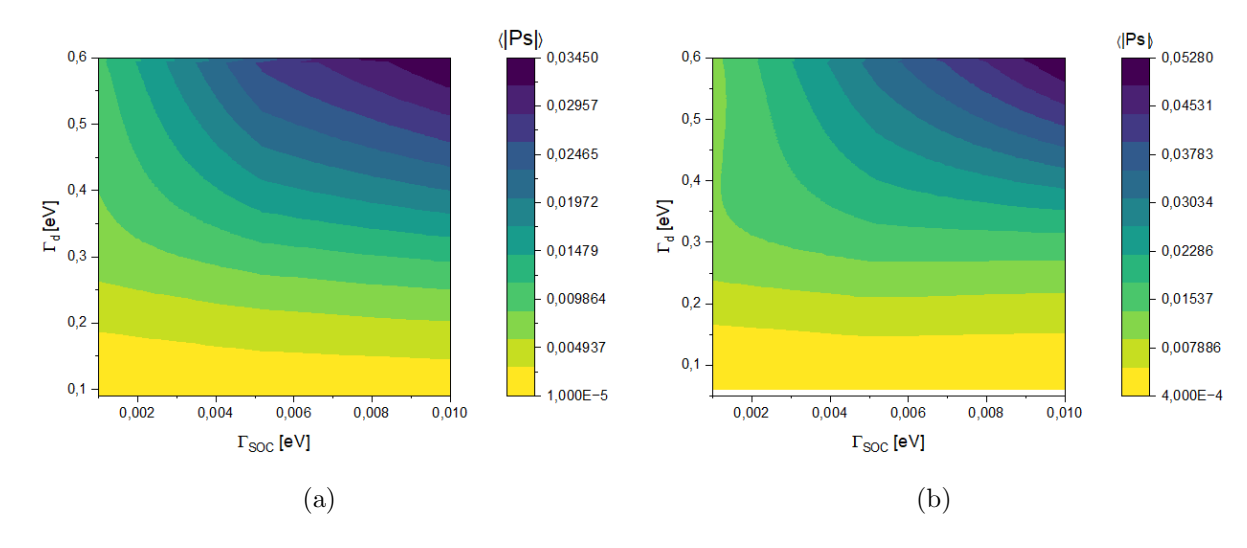


Figure 3.5: Spin polarization as a function of the spin-orbit strength and the dephasing coupling strength (a) without a barrier (b) with a barrier intensity of 1 eV.

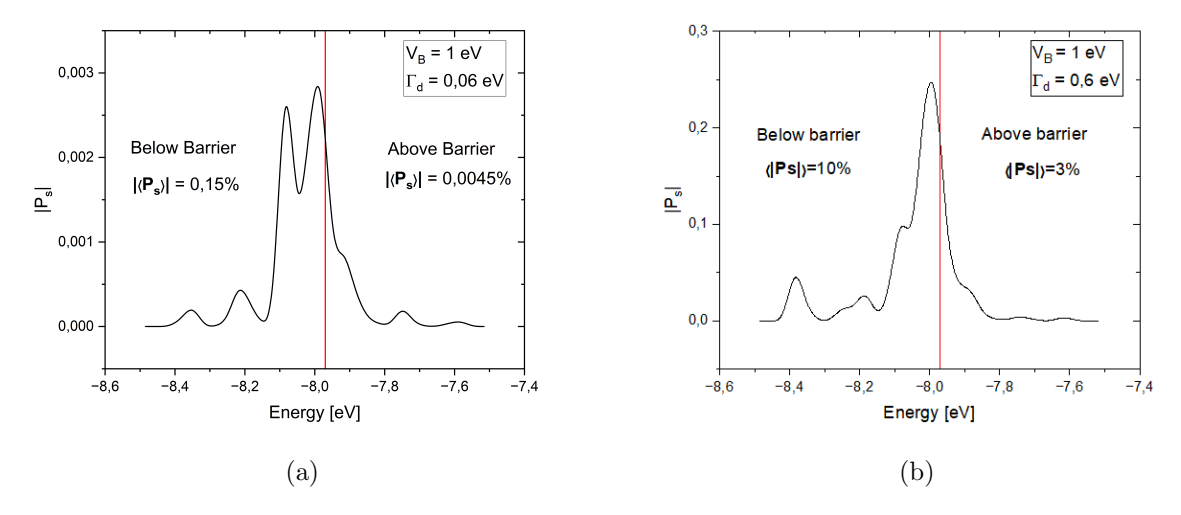


Figure 3.6: Spin polarization as a function of the energy injection with (a) a barrier of intensity  $V_B = 1 \ eV$  with decoherence strength  $\Gamma_d = 0.06 \ eV$  (b) a barrier of intensity  $V_B = 1 \ eV$  with decoherence strength  $\Gamma_d = 0.6 \ eV$ .

Referring to the energy scheme in Figure 2.3 (a), spin polarization is higher when the injection energy is below the barrier. Figure 3.6 a) shows that the average spin polarization increases to approximately 0.15~% below the barrier and then declines to about 0.0045~% above it, marking a substantial change of two orders of magnitude. In Figure 3.6 b), with

a higher dephasing coupling ( $\Gamma_d = 0.6 \ eV$ ), spin polarization rises to nearly 10 % below the barrier and drops to around 3 % above it.

#### 3.2 Spin Polarization in dsDNA

The electron transmission behavior in dsDNA requires a more detailed analysis than that of ssDNA. Specifically, the energy difference between the Adenine-HOMO and Thymine-LUMO strands plays a significant role in shaping the electron transmission profile, depending on whether the leads are connected symmetrically or asymmetrically to the molecule. To study this, a toy model of three base pairs was simulated. Decoherence leads were connected to all sites with a decoupling strength of  $\Gamma_d = 0.06 \ eV$ , the chemical potential of the leads was set as the average of the HOMO and LUMO energies,  $(\mu = -6.5 \text{ eV})$ , and the coupling of the electrodes to the system is set to  $V_{tR} = V_{tL} = 1 \text{ eV}$ . Figure 3.7 illustrates the conductance profiles for all possible lead connections. In panel (a), the conductances are shifted: when the leads are connected to the Adenine-HOMO strand, the conductance peak is centered at -8.2 eV, whereas when connected to the Thymine-LUMO strand, the peak shifts to -4.8 eV. This is because the accessible states for electron transmission are related to the energy sites of the molecule. Panel (b) shows that the conductance decreases by three orders of magnitude when the leads are connected asymmetrically. This is because the LUMO energy acts as a barrier that the electron needs to travel in order to be transmitted.

The energy difference between the Adenine-HOMO and Thymine-LUMO strands also affects spin polarization. Figure 3.8 shows that around the HOMO energy, the conductance is approximately  $\sim 0.01~e^2/h$  with a spin polarization close to 0.07 %. In contrast, near the LUMO energy, the conductance decreases significantly to around  $1E-7~e^2/h$  while the spin polarization rises to 0.15 %. This demonstrates a resonant versus a non-resonant effect, similar to the behavior of electrons tunneling below a barrier: while the conductance remains low, the system still displays substantial spin polarization. Here, the LUMO energy acts as a barrier, enabling additional channels for conduction and spin polarization that differ from the results observed in ssDNA, where the site energies are

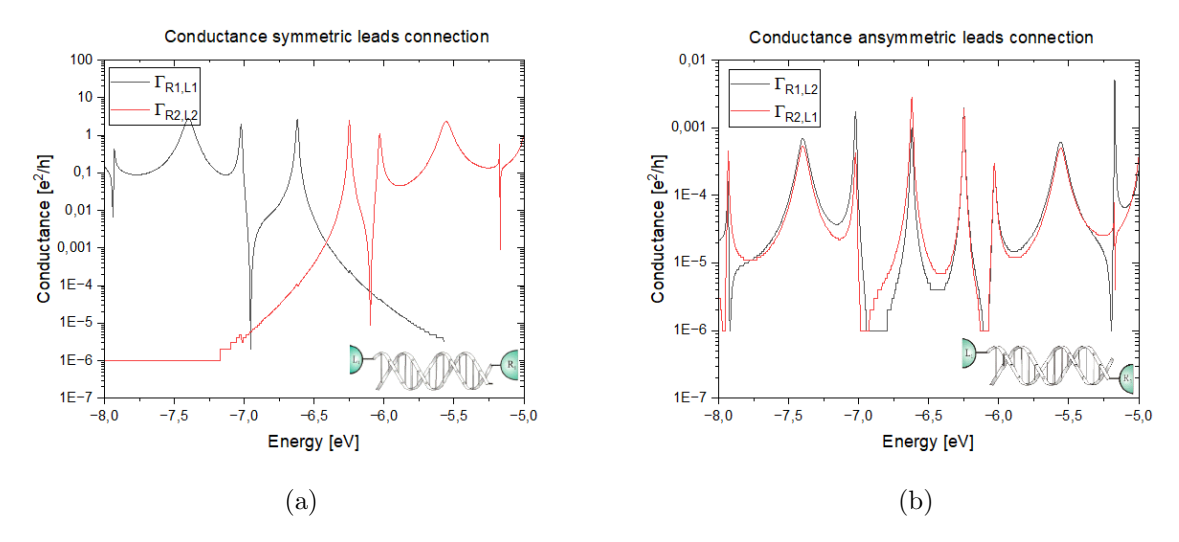


Figure 3.7: Conductance with (a) symmetric connections to the left and right leads: Adenine-HOMO strand (black) and Thymine-LUMO strand (red), and (b) asymmetric connections to the left and right leads.

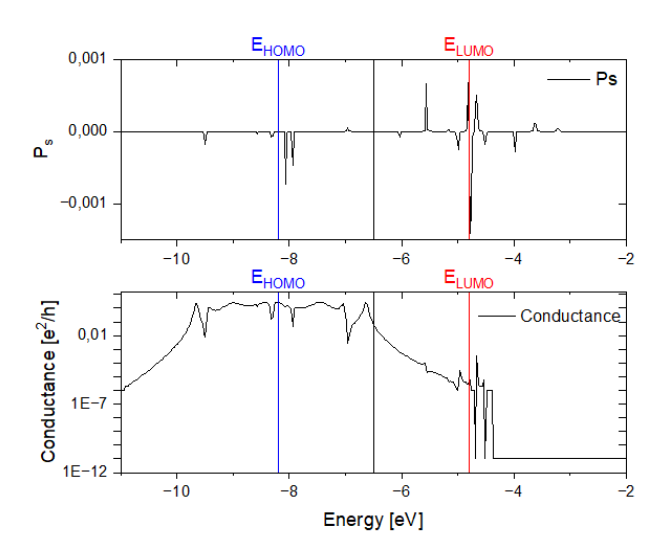
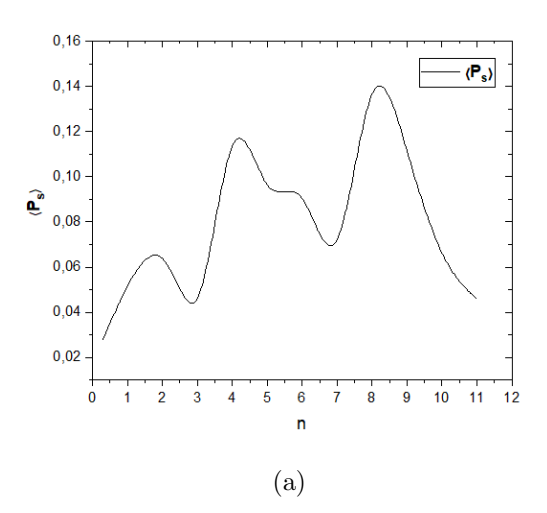


Figure 3.8: Spin polarization (above panel) and conductance (below panel) in a DNA toy model of 3 pair bases as a function of the injection energy of the leads.

#### homogenous.

Figure 3.9 presents the average spin polarization as a function of the number of turns and the coupling strength of the dephasing probe. The behavior closely resembles that observed in ssDNA: spin polarization generally increases with the number of turns, though not in a strictly monotonic manner. Additionally, average spin polarization peaks at approximately 15 % when the dephasing strength reaches  $0.5\ eV$  after which it declines as inelastic events begin to interfere with electron transmission.



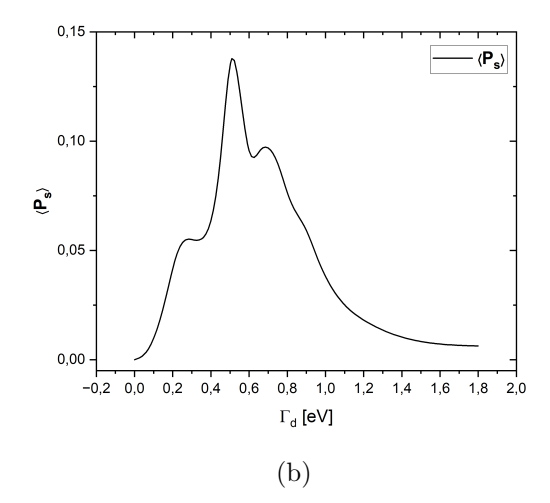
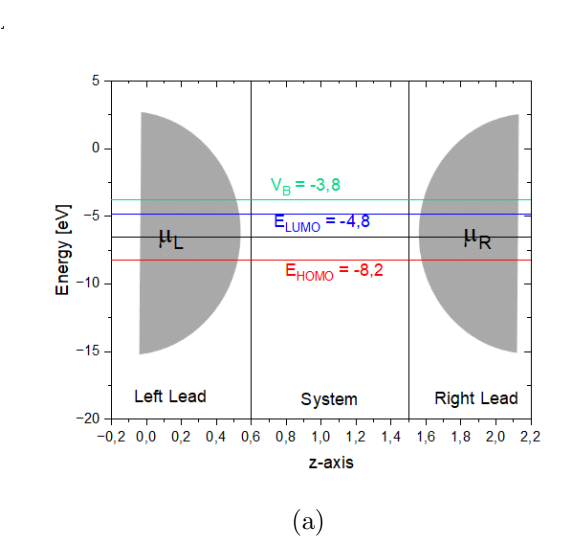


Figure 3.9: Averaged spin polarization in DNA in as a function of (a) number of turns (n) (b) the coupling strength of the dephasing probe to the system.

#### 3.2.1 Tunneling effect



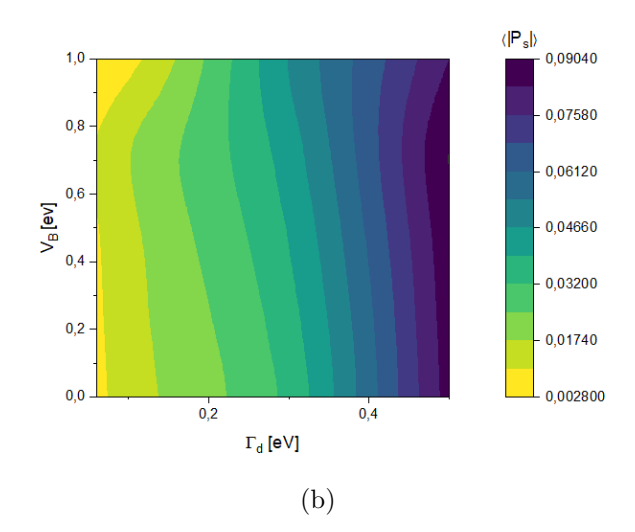


Figure 3.10: (a) Energy scheme of the injection energies in the leads, the energy of the system, and the barrier intensity. (b) Average spin polarization as a function of the barrier intensity  $(V_B)$  and the dephasing coupling strength  $(\Gamma_d)$  in the DNA model.

To evaluate the effect of the barrier in dsDNA, a model consisting of 30 base pairs (60 sites) was simulated, with decoherence probes connected to all sites. This setup was chosen because, when only one probe is connected to the system, spin polarization appears only at specific energies, depending on whether the decoherence probe was attached to the HOMO strand or the LUMO strand. Figure 3.10 illustrates how spin polarization

is enhanced with the barrier intensity and decoupling strength while conductance drops. It is important to note that this enhancement is not as regular as in the case of ssDNA due to interference effects. Nevertheless, the slight inclination to the left of the pattern indicates that spin polarization grows when the dephasing coupling strength is maintained while the barrier is increased. Additionally, the maximum spin polarization in dsDNA exceeds that in ssDNA, as expected, given the inclusion of multiple decoherence probes in the system.

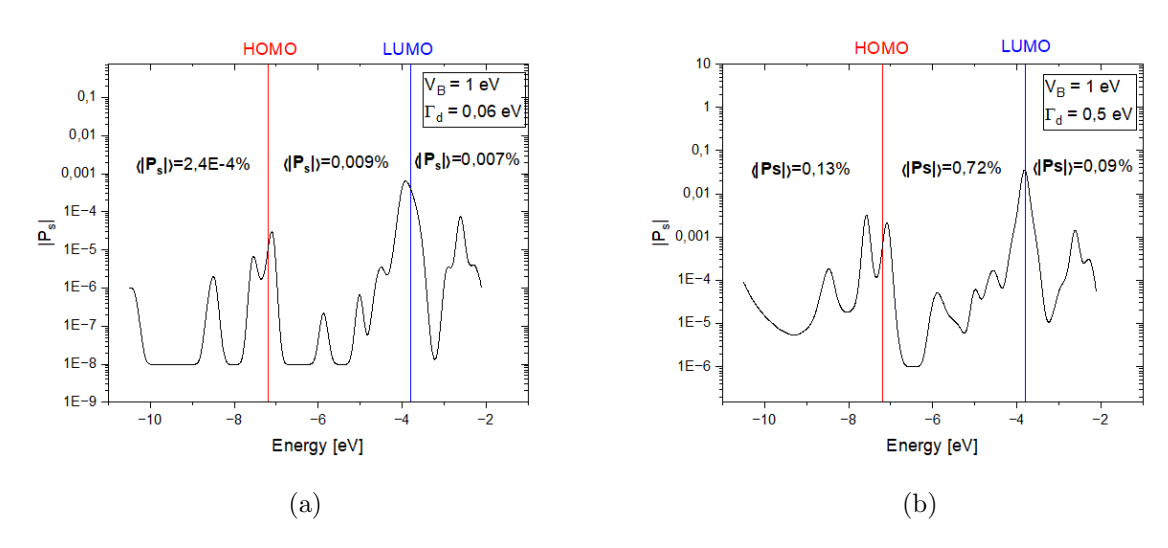


Figure 3.11: Average spin polarization as a function of the injection energy around a barrier of 1 eV (a) with a dephasing coupling strength of  $\Gamma_d = 0.06 \ eV$  (b) with a dephasing coupling strength of  $\Gamma_d = 0.5 \ eV$ 

Figure 3.11 shows the spin polarization as a function of the injection energy near the barrier. In both cases, the spin polarization reaches a maximum when the injection energy is between the HOMO and LUMO barriers and decreases when the injection energy is above the highest LUMO barrier. This detrimental effect reaches two orders of magnitude when the dephasing coupling strength is comparable to the couplings in the molecule, in agreement with the results presented for the ssDNA 3.6. This is the typical behavior of the tunnel effect, and once again, the spin polarization is enhanced by the presence of a barrier in the system. The difference when the dephasing coupling is smaller is not significant, but note that in general, the spin polarization is several orders of magnitude smaller than in the other case. The combined effects of the barrier and dephasing also influence the conductance, which decreases to  $10^{-6} e^2/h$  with minimal dephasing coupling

and further drops to  $10^{-9} e^2/h$  at maximum dephasing. This behavior is analogous to the resonant and non-resonant effects observed in DNA without a barrier, where conductance decreases at certain energies while spin polarization increases.

#### 3.3 Band Folding

After implementing the effective Hamiltonian of Eq. 2.54 in Kwant for a 3-site helix, the spin polarization decreased by several orders of magnitude to approximately  $\sim 10^{-10}$  %, while the conductance exhibited similar peaks to those observed in the complete orbital model. Considering that models in the literature [58] use this approximation with Hamiltonians in reciprocal space, it appears that the band-folding method is incompatible with finite systems: Although the quantum number k is well-defined in the semi-infinite leads, as demonstrated in the methods section, it is not well-defined within the finite system itself, even if the energies are. For this reason, a reciprocal-space version of the model was constructed, but its analysis in terms of spin behavior is deferred to future work.

For simplicity, the Hamiltonian describing the interaction between two sites with bare spin-orbit and kinetic coupling was constructed as follows:

|                    | $ p_{zi}\rangle$      | $ p_{zj}\rangle$      | $ s_i\rangle$ | $ p_{xi}\rangle$      | $ p_{yi}\rangle$      | $ s_j\rangle$ | $ p_{xj}\rangle$      | $ p_{yj}\rangle$      |
|--------------------|-----------------------|-----------------------|---------------|-----------------------|-----------------------|---------------|-----------------------|-----------------------|
| $\langle p_{zi} $  | $\epsilon_p^\pi$      | $E_{zz}$              | 0             | $-i\lambda \hat{s}_y$ | $i\lambda \hat{s}_x$  | 0             | $E_{xz}$              | $E_{yz}$              |
| $\langle p_{zj} $  | $E_{zz}$              | $\epsilon_p^\pi$      | 0             | $E_{xz}$              | $E_{yz}$              | 0             | $-i\lambda \hat{s}_y$ | $i\lambda \hat{s}_x$  |
| $\langle s_i  $    | 0                     | 0                     | $\epsilon_s$  | 0                     | 0                     | 0             | 0                     | 0                     |
| $\langle p_{xi} $  | $i\lambda \hat{s}_y$  | $E_{xz}$              | 0             | $\epsilon_p^\sigma$   | $-i\lambda \hat{s}_z$ | 0             | 0                     | 0                     |
| $\langle p_{y_i} $ | $-i\lambda \hat{s}_x$ | $E_{yz}$              | 0             | $i\lambda \hat{s}_z$  | $E_p^{\sigma}$        | 0             | 0                     | 0                     |
| $\langle s_j  $    | 0                     | 0                     | 0             | 0                     | 0                     | $\epsilon_s$  | 0                     | 0                     |
| $\langle p_{xj} $  | $E_{xz}$              | $i\lambda \hat{s}_y$  | 0             | 0                     | 0                     | 0             | $\epsilon_p^\sigma$   | $-i\lambda \hat{s}_z$ |
| $\langle p_{yj} $  | $E_{yz}$              | $-i\lambda \hat{s}_x$ | 0             | 0                     | 0                     | 0             | $i\lambda \hat{s}_z$  | $\epsilon_p^\sigma$   |

After applying the transformation:

$$H_{eff} = H_{\pi} - TH_{\pi}^{-1}T^{\dagger}, \tag{3.1}$$

the effective Hamiltonian can be written in the form

$$\begin{array}{c|cc}
 & |p_{zi}\rangle & |p_{zj}\rangle \\
\hline
\langle p_{zi}| & E'_s & V'_{zz} \\
\langle p_{zj}| & V'_{zz} & E'_s
\end{array}$$

where

$$E'_{s} = \epsilon_{p}^{\pi} - \frac{(\epsilon_{p}^{\sigma} E_{xz} - i\lambda E_{yz} s_{z}) E_{xz} - (\epsilon_{p}^{\sigma} E_{yz} - i\lambda E_{xz} s_{z}) E_{yz} - 2\lambda^{2} \epsilon_{p}^{\sigma}}{\epsilon_{p}^{\sigma^{2}} - \lambda^{2}},$$

$$V'_{zz} = E_{zz} - \frac{-2i\lambda \epsilon_{p}^{\sigma} s_{y} E_{xz} + 2i\lambda \epsilon_{p}^{\sigma} s_{x} E_{yz}}{\epsilon_{p}^{\sigma^{2}} - \lambda^{2}},$$

The Hamiltonian in reciprocal space is defined by:

$$\mathcal{H}(k) = \frac{1}{N} \sum_{i=1}^{N} \sum_{j=1}^{N} e^{i\mathbf{k}\mathbf{R}_{ij}} \langle \Phi_i | \mathcal{H} | \Phi_j \rangle$$
(3.2)

$$= \frac{1}{N} \left( \sum_{i=j}^{N} \langle \Phi_i | \mathcal{H} | \Phi_j \rangle + \sum_{i \neq j}^{N} e^{i \mathbf{k} \mathbf{R}_{ij}} \langle \Phi_i | \mathcal{H} | \Phi_j \rangle \right), \tag{3.3}$$

where  $\mathbf{R}_{ij} = \mathbf{R}$  is the distance between two sites and is the same for every i, j.

It is important to note that the phase in the diagonal terms is zero, as these terms involve processes occurring within orbitals of the same site. In contrast, the off-diagonal terms acquire a phase that depends on the transitions between orbitals of different sites. The reciprocal Hamiltonian can thus be expressed in the following form:

$$\mathcal{H}(k) = E_s^{\pi} + E_{zz} f(\mathbf{k}) - \frac{-2i\lambda \epsilon_p^{\sigma} s_y E_{xz} + 2i\lambda \epsilon_p^{\sigma} s_x E_{yz}}{\epsilon_p^{\sigma^2} - \lambda^2} g(\mathbf{k})$$
(3.4)

where

$$f(\mathbf{k}) = 2\cos(\mathbf{k} \cdot \mathbf{R}),\tag{3.5}$$

$$g(\mathbf{k}) = 2\sin(\mathbf{k} \cdot \mathbf{R}). \tag{3.6}$$

The new Hamiltonian in reciprocal space can be evaluated in a k point in the Brillouin

zone, typically around a hall-full k point.

# Chapter 4

### Conclusions

This work introduced a tight-binding model to analyze charge transport and spin polarization in chiral systems, specifically single-stranded DNA (ssDNA) and double-stranded DNA (dsDNA). Unlike other tight-binding models, this approach incorporated a detailed description of s- and p-orbitals at each site. This level of detail allowed for the emergence of intrinsic spin-orbit coupling (SOC), the Stark effect, and the Rashba effect, arising naturally from the orbital geometry and their overlaps in the helical structure. Additionally, the model did not exhibit spin polarization in a two-terminal setup, consistent with Onsager's reciprocity relations, necessitating the introduction of a third probe to incorporate decoherence.

The results are promising and remark the importance of geometrical considerations in the theoretical models for understanding CISS. First, the strength of the SOC used was the intrinsic atomic value, as measured experimentally, and there was no need to artificially adjust this parameter above meV magnitudes to achieve spin polarization. This provides a more accurate description of CISS compared to existing models. Second, the orbital model demonstrated spin polarization in ssDNA without requiring interactions with additional nearest neighbors, with results several orders of magnitude higher than those reported in the literature. This highlights the critical importance of geometric parameters in theoretical models analyzing CISS.

The role of decoherence was also examined. The highest spin polarization values were observed when the dephasing coupling strength was comparable to the coupling

parameters within the system. Introducing decoherence probes not only broke timereversal symmetry but also played a crucial role in enabling spin accumulation. However, excessive increases in the dephasing coupling negatively impacted electron transmission and spin polarization, as electrons tended to escape through the reservoir.

Electron behavior in ssDNA and dsDNA was analyzed within the tunneling and hopping regimes. For ssDNA, where the site energies are uniform along the molecule, spin polarization aligned with the resonant conductance peaks. In dsDNA, the energy difference between strands significantly influenced electron transmission, producing resonant peaks near the HOMO energy and non-resonant peaks near the LUMO strand. The LUMO strand acted as a barrier that enhanced spin polarization. Furthermore, adding an external potential barrier affected spin polarization in both cases, demonstrating that spin polarization is maximized when the injection energy is below the barrier and decreases when it is above it.

#### 4.1 Future work

Several important aspects were not addressed in this study and warrant further exploration: First, the introduction of decoherence leads as a source of leakage of probability results in the loss of unitarity in the system's transmission. Testing the model with a more sophisticated approach for incorporating decoherence, such as the D'Amato-Pastawski formalism, could maintain unitarity while still breaking time-reversal symmetry, offering a more subtle representation of decoherence effects.

Concerning the spin-active paths in the double helical system, recent group theory studies of line groups have revealed spin-active channels between helices that should be included in a complete orbital model [59, 60]. Also, the inversion asymmetry of the helix (and of all chiral structures) makes for an internal potential that contributes to an intrinsic Rashba term that has not been considered here. Such a coupling is distinguished from the Rashba effect coming from hydrogen bonding and is important to determine intrinsic from extrinsic spin effects.

Additionally, a Hamiltonian in reciprocal space was developed using the band-folding

methodology, as the folded Hamiltonian in real space did not provide a reliable framework for qualitatively analyzing spin behavior in the system. This reciprocal space approach can potentially deepen the understanding of CISS, particularly as it remains underexplored in other studies.

# **Bibliography**

- [1] Matthias Geyer, Rafael Gutierrez, and Gianaurelio Cuniberti. Effective hamiltonian model for helically constrained quantum systems within adiabatic perturbation theory: Application to the chirality-induced spin selectivity (ciss) effect. *The Journal of chemical physics*, 152(21), 2020.
- [2] Karen Michaeli and Ron Naaman. Origin of spin-dependent tunneling through chiral molecules. *The Journal of Physical Chemistry C*, 123(27):17043–17048, 2019.
- [3] Ricardo Gutierrez, E Diaz, Ron Naaman, and G Cuniberti. Spin-selective transport through helical molecular systems. *Physical Review B—Condensed Matter and Materials Physics*, 85(8):081404, 2012.
- [4] Ai-Min Guo and Qing-feng Sun. Spin-selective transport of electrons in dna double helix. *Physical review letters*, 108(21):218102, 2012.
- [5] Ai-Min Guo and Qing-Feng Sun. Spin-dependent electron transport in proteinlike single-helical molecules. Proceedings of the National Academy of Sciences, 111(32):11658–11662, 2014.
- [6] Ai-Min Guo, Ting-Rui Pan, Tie-Feng Fang, XC Xie, and Qing-Feng Sun. Spin selectivity effect in achiral molecular systems. *Physical Review B*, 94(16):165409, 2016.
- [7] Xu Yang, Caspar H van der Wal, and Bart J van Wees. Detecting chirality in two-terminal electronic nanodevices. *Nano letters*, 20(8):6148–6154, 2020.

- [8] Laurence George Demosthenis Hawke, George Kalosakas, and Constantinos Simserides. Electronic parameters for charge transfer along dna. *The European Physical Journal E*, 32(3):291–305, 2010.
- [9] Brian P Bloom, Yossi Paltiel, Ron Naaman, and David H Waldeck. Chiral induced spin selectivity. *Chemical Reviews*, 124(4):1950–1991, 2024.
- [10] Nevill Francis Mott. The electrical conductivity of transition metals. Proceedings of the Royal Society of London. Series A-Mathematical and Physical Sciences, 153(880):699-717, 1936.
- [11] Nevill Francis Mott. The resistance and thermoelectric properties of the transition metals. Proceedings of the Royal Society of London. Series A-Mathematical and Physical Sciences, 156(888):368–382, 1936.
- [12] Igor Žutić, Jaroslav Fabian, and S Das Sarma. Spintronics: Fundamentals and applications. *Reviews of modern physics*, 76(2):323, 2004.
- [13] PS Farago. Spin-dependent features of electron scattering from optically active molecules. *Journal of Physics B: Atomic and Molecular Physics*, 13(18):L567, 1980.
- [14] Stefan Mayer and Joachim Kessler. Experimental verification of electron optic dichroism. *Physical review letters*, 74(24):4803, 1995.
- [15] K Blum, M Musigmann, and D Thompson. Elastic electron collision with chiral and oriented molecules. In Supercomputing, Collision Processes, and Applications, pages 137–153. Springer, 1999.
- [16] K Ray, SP Ananthavel, DH Waldeck, and Ron Naaman. Asymmetric scattering of polarized electrons by organized organic films of chiral molecules. *Science*, 283(5403):814–816, 1999.
- [17] Clarice D Aiello, John M Abendroth, Muneer Abbas, Andrei Afanasev, Shivang Agarwal, Amartya S Banerjee, David N Beratan, Jason N Belling, Bertrand Berche,

- Antia Botana, et al. A chirality-based quantum leap. ACS nano, 16(4):4989-5035, 2022.
- [18] Suryakant Mishra, Amit Kumar Mondal, Shubhadeep Pal, Tapan Kumar Das, Eilam ZB Smolinsky, Giuliano Siligardi, and Ron Naaman. Length-dependent electron spin polarization in oligopeptides and dna. The Journal of Physical Chemistry C, 124(19):10776–10782, 2020.
- [19] Neeraj Bangruwa, Manish Srivastava, and Debabrata Mishra. Ciss-based label-free novel electrochemical impedimetric detection of uvc-induced dna damage. ACS Omega, 7(42):37705–37713, 2022.
- [20] Prashant K Bhartiya, Suryansh, Neeraj Bangruwa, Manish Srivastava, and Debabrata Mishra. Light-amplified ciss-based hybrid qd-dna impedimetric device for dna hybridization detection. Analytical Chemistry, 95(7):3656–3665, 2023.
- [21] Bernd Giese. Electron transfer in dna. Current opinion in chemical biology, 6(5):612–618, 2002.
- [22] Stuart Lindsay. Ubiquitous electron transport in non-electron transfer proteins. *Life*, 10(5):72, 2020.
- [23] Zouti Xie, Tal Z Markus, Sidney R Cohen, Zeev Vager, Rafael Gutierrez, and Ron Naaman. Spin specific electron conduction through dna oligomers. Nano letters, 11(11):4652–4655, 2011.
- [24] Dominik M Stemer, John M Abendroth, Kevin M Cheung, Matthew Ye, Mohammed S El Hadri, Eric E Fullerton, and Paul S Weiss. Differential charging in photoemission from mercurated dna monolayers on ferromagnetic films. *Nano letters*, 20(2):1218–1225, 2020.
- [25] Itai Carmeli, Karuppannan Senthil Kumar, Omri Heifler, Chanoch Carmeli, and Ron Naaman. Spin selectivity in electron transfer in photosystem i. Angewandte Chemie International Edition, 53(34):8953–8958, 2014.

- [26] Vankayala Kiran, Shinto P Mathew, Sidney R Cohen, Irene Hernandez Delgado, Jérôme Lacour, and Ron Naaman. Helicenes—a new class of organic spin filter. Advanced Materials, 28(10):1957–1962, 2016.
- [27] Niccolo Giaconi, Lorenzo Poggini, Michela Lupi, Matteo Briganti, Anil Kumar, Tapan K Das, Andrea L Sorrentino, Caterina Viglianisi, Stefano Menichetti, Ron Naaman, et al. Efficient spin-selective electron transport at low voltages of thiabridged triarylamine hetero [4] helicenes chemisorbed monolayer. ACS nano, 17(15):15189–15198, 2023.
- [28] Rafael Rodríguez, Cristina Naranjo, Anil Kumar, Paola Matozzo, Tapan Kumar Das, Qirong Zhu, Nicolas Vanthuyne, Rafael Gómez, Ron Naaman, Luis Sánchez, et al. Mutual monomer orientation to bias the supramolecular polymerization of [6] helicenes and the resulting circularly polarized light and spin filtering properties.

  Journal of the American Chemical Society, 144(17):7709–7719, 2022.
- [29] Amit Kumar Mondal, Marco D Preuss, Marcin L Sleczkowski, Tapan Kumar Das, Ghislaine Vantomme, EW Meijer, and Ron Naaman. Spin filtering in supramolecular polymers assembled from achiral monomers mediated by chiral solvents. *Journal of the American Chemical Society*, 143(18):7189–7195, 2021.
- [30] Lei Jia, Chenchen Wang, Yuchun Zhang, Liu Yang, and Yong Yan. Efficient spin selectivity in self-assembled superhelical conducting polymer microfibers. ACS nano, 14(6):6607–6615, 2020.
- [31] B Gohler, V Hamelbeck, TZ Markus, M Kettner, GF Hanne, Zeev Vager, Ron Naaman, and H Zacharias. Spin selectivity in electron transmission through self-assembled monolayers of double-stranded dna. Science, 331(6019):894–897, 2011.
- [32] M Kettner, B Gohler, H Zacharias, D Mishra, V Kiran, R Naaman, Claudio Fontanesi, David H Waldeck, Slawomir Sek, Jan Pawlowski, et al. Spin filtering in electron transport through chiral oligopeptides. The Journal of Physical Chemistry C, 119(26):14542–14547, 2015.

- [33] Y Lu, BP Bloom, S Qian, and DH Waldeck. Enantiospecificity of cysteine adsorption on a ferromagnetic surface: Is it kinetically or thermodynamically controlled? *The Journal of Physical Chemistry Letters*, 12(32):7854–7858, 2021.
- [34] Paul V Mollers, Jimeng Wei, Soma Salamon, Manfred Bartsch, Heiko Wende, David H Waldeck, and Helmut Zacharias. Spin-polarized photoemission from chiral cuo catalyst thin films. ACS nano, 16(8):12145–12155, 2022.
- [35] KB Ghosh, Wenyan Zhang, F Tassinari, Y Mastai, O Lidor-Shalev, R Naaman, P Mollers, D Nurenberg, H Zacharias, J Wei, et al. Controlling chemical selectivity in electrocatalysis with chiral cuo-coated electrodes. *The Journal of Physical Chemistry* C, 123(5):3024–3031, 2019.
- [36] Yingdan Xu and Wenbo Mi. Chiral-induced spin selectivity in biomolecules, hybrid organic–inorganic perovskites and inorganic materials: a comprehensive review on recent progress. *Materials Horizons*, 10(6):1924–1955, 2023.
- [37] Matthias Geyer, Rafael Gutierrez, Vladimiro Mujica, and Gianaurelio Cuniberti. Chirality-induced spin selectivity in a coarse-grained tight-binding model for helicene.

  The Journal of Physical Chemistry C, 123(44):27230–27241, 2019.
- [38] Ramon Torres-Cavanillas, Garin Escorcia-Ariza, Isaac Brotons-Alcazar, Roger Sanchis-Gual, Prakash Chandra Mondal, Lorena E Rosaleny, Silvia Gimenez-Santamarina, Michele Sessolo, Marta Galbiati, Sergio Tatay, et al. Reinforced room-temperature spin filtering in chiral paramagnetic metallopeptides. *Journal of the American Chemical Society*, 142(41):17572–17580, 2020.
- [39] Sina Yeganeh, Mark A Ratner, Ernesto Medina, and Vladimiro Mujica. Chiral electron transport: Scattering through helical potentials. *The Journal of chemical physics*, 131(1), 2009.
- [40] Solmar Varela, Ernesto Medina, Floralba Lopez, and Vladimiro Mujica. Inelastic electron scattering from a helical potential: transverse polarization and the structure

- factor in the single scattering approximation. *Journal of Physics: Condensed Matter*, 26(1):015008, 2013.
- [41] Ernesto Medina, Floralba Lopez, Mark A Ratner, and Vladimiro Mujica. Chiral molecular films as electron polarizers and polarization modulators. *Europhysics Let*ters, 99(1):17006, 2012.
- [42] Dhurba Rai and Michael Galperin. Electrically driven spin currents in dna. *The Journal of Physical Chemistry C*, 117(26):13730–13737, 2013.
- [43] Solmar Varela, Vladimiro Mujica, and Ernesto Medina. Effective spin-orbit couplings in an analytical tight-binding model of dna: Spin filtering and chiral spin transport. Physical Review B, 93(15):155436, 2016.
- [44] Volodymyr V Maslyuk, Rafael Gutierrez, Arezoo Dianat, Vladimiro Mujica, and Gianaurelio Cuniberti. Enhanced magnetoresistance in chiral molecular junctions. The journal of physical chemistry letters, 9(18):5453–5459, 2018.
- [45] Elena Diaz, Francisco Dominguez-Adame, Rafael Gutierrez, Gianaurelio Cuniberti, and Vladimiro Mujica. Thermal decoherence and disorder effects on chiral-induced spin selectivity. The journal of physical chemistry letters, 9(19):5753–5758, 2018.
- [46] Christoph W Groth, Michael Wimmer, Anton R Akhmerov, and Xavier Waintal. Kwant: a software package for quantum transport. New Journal of Physics, 16(6):063065, 2014.
- [47] Miguel Mena, Solmar Varela, Bertrand Berche, and Ernesto Medina. Minimal model for chirally induced spin selectivity: spin-orbit coupling, tunneling and decoherence. Journal of Statistical Mechanics: Theory and Experiment, 2024(8):084001, 2024.
- [48] XF Wang and Tapash Chakraborty. Charge transfer via a two-strand superexchange bridge in dna. *Physical review letters*, 97(10):106602, 2006.

- [49] Mayra Peralta, Steven Feijoo, Solmar Varela, Rafael Gutierrez, Gianaurelio Cuniberti, Vladimiro Mujica, and Ernesto Medina. Spin-phonon coupling in a double-stranded model of dna. *The Journal of Chemical Physics*, 159(2), 2023.
- [50] Natallia V Grib, Dmitry A Ryndyk, Rafael Gutiérrez, and Gianaurelio Cuniberti. Distance-dependent coherent charge transport in dna: crossover from tunneling to free propagation. *Journal of Biophysical Chemistry*, 1(02):77–85, 2010.
- [51] R Gutierrez and G Cuniberti. Spin-dependent effects in helical molecular systems with rashba-like spin-orbit interaction. Acta Physica Polonica A, 127(2):185–191, 2015.
- [52] Horacio M Pastawski and Ernesto Medina. Tight binding'methods in quantum transport through molecules and small devices: From the coherent to the decoherent description. arXiv preprint cond-mat/0103219, 2001.
- [53] Daniel S Fisher and Patrick A Lee. Relation between conductivity and transmission matrix. *Physical Review B*, 23(12):6851, 1981.
- [54] Xu Yang. Connecting chirality and spin in electronic devices. 2020.
- [55] Xu Yang, Caspar H. van der Wal, and Bart J. van Wees. Detecting chirality in two-terminal electronic nanodevices. *Nano Letters*, 20(8):6148–6154, 2020. PMID: 32672980.
- [56] Leslie L Foldy and Siegfried A Wouthuysen. On the dirac theory of spin 1/2 particles and its non-relativistic limit. *Physical Review*, 78(1):29, 1950.
- [57] Limin Xiang, Julio L Palma, Christopher Bruot, Vladimiro Mujica, Mark A Ratner, and Nongjian Tao. Intermediate tunnelling-hopping regime in dna charge transport. Nature chemistry, 7(3):221–226, 2015.
- [58] Edward McCann and Mikito Koshino. The electronic properties of bilayer graphene.

  Reports on Progress in physics, 76(5):056503, 2013.

- [59] Pablo Mendieta. Spin transport hamiltonians on molecular helices: Derivations from symmetry, 2024.
- [60] Denis Kochan, Susanne Irmer, and Jaroslav Fabian. Model spin-orbit coupling hamiltonians for graphene systems. *Physical Review B*, 95(16):165415, 2017.

# Appendix A: Discretization Aquiral Nanotubes Model

$$\mathcal{H} = \mathcal{H}_0 + \mathcal{H}_{el} + \mathcal{H}_d, \tag{4.1}$$

$$\mathcal{H}_0 = \frac{\hat{p}}{2m} + \hat{V} + \frac{\hbar}{4m^2c^2} \nabla V(\hat{\sigma} \times \hat{p}),$$

Consider that  $\psi$  are the eigenstates of the Hamiltonian of the system:

$$\mathcal{H}_0\psi = E\psi$$
,

It is possible to rewrite the operator  $\hat{p}$  in its differential form:

$$\hat{p}^2 = -\hbar^2 (\partial_x^2 + \partial_y^2 + \partial_z^2),$$

$$-\frac{\hbar^2}{2m} \partial_i \psi_i + \hat{V}\psi_i + \vec{\gamma}(\hat{\sigma} \times \partial_i) = E\psi,$$
(4.2)

where  $\vec{\gamma} = \nabla V$ 

$$\partial_j^2 \psi_j = \frac{\psi_{(j+\Delta j)} - 2\psi_j + \psi_{(j-\Delta j)}}{\Delta_j^2}, \qquad j = x, y$$

$$\partial_n^2 \psi_n = \frac{\psi_{(n+\Delta n)} - 2\psi_n + \psi_{(n-\Delta n)}}{\Delta_n^2}, \qquad n = z$$

while the SOC term can be written in the form:

$$\vec{\gamma}(\hat{\sigma} \times \hat{p}) = -\vec{\gamma}\epsilon_{ijk}\sigma_j\hbar i\partial_k(\psi_{nj}) \tag{4.3}$$

$$= -i\hbar \vec{\gamma} \sigma_j \partial_k \psi_{nj} \tag{4.4}$$

where we use the central derivative in finite differences:

$$\partial_i \psi_i = \frac{\psi_{(i+\Delta i)} - \psi_{(i-\Delta i)}}{2\Delta_i}$$

replacing the finite differences in 4.2

$$-\frac{\hbar^{2}}{2m\Delta_{j}^{2}}(u_{j+1,n}-2u_{jn}+u_{j-1,n})-\frac{\hbar^{2}}{2m\Delta_{n}^{2}}(u_{j,n+1}-2u_{jn}+u_{j,n-1})+\hat{V}-i(\hbar/4m^{2}c^{2})\hbar\gamma_{y}$$

$$\left[\epsilon_{yxz}\sigma_{j}(\frac{u_{j,n+1-u_{j,n-1}}}{2\Delta_{n}})+\epsilon_{yzx}\sigma_{z}(\frac{u_{j+1,n-u_{j-1,n}}}{2\Delta_{j}})\right] (4.5)$$

we have considered  $\vec{\gamma} = \gamma \hat{j}$  th electric field is in the radial direction:

$$t_{\parallel}(u_{j+1,n} - 2u_{jn} + u_{j-1,n}) + t_{\perp}(u_{j,n+1} - 2u_{jn} + u_{j,n-1}) + Vu_{jn} + is\sigma_{i}(u_{j,n+1} - u_{j,n-1}) - i\mu\sigma_{z}(u_{j+1,n} - u_{j-1,n})$$
(4.6)

rewriting the  $u_{jn}$  as a  $|j,n\rangle$  state

$$t_{\parallel}(|j+1,n\rangle\langle j,n|-2|j,n\rangle\langle j,n|+|j,n\rangle\langle j+1,n|)+t_{\perp}(|j,n+1\rangle\langle j,n|-2|j,n\rangle\langle j,n|+|j,n\rangle\langle j,n|+|j,n\rangle\langle j,n+1|)+V|j,n\rangle\langle j,n|+is\sigma_{j}(|j,n+1\rangle\langle j,n|-|j,n\rangle\langle j,n+1|)-i\mu\sigma_{z}(|j+1,n\rangle\langle j,n|-|j,n\rangle\langle j+1,n|)$$
(4.7)

Rewriting everything in terms of the creation and annihilation operators:

$$H_{0} = \sum_{j=1}^{J} \left[ \sum_{n=1}^{N} \epsilon_{jn} c_{jn}^{\dagger} c_{jn} + \sum_{n=1}^{N-1} c_{jn}^{\dagger} (t_{\parallel} + 2is\sigma_{j}) c_{j,n+1} + \sum_{n=1}^{N} c_{jn}^{\dagger} (t_{\perp} + 2i\mu\sigma_{z}) c_{j+1,n} + H.c. \right],$$

$$(4.8)$$

# Appendix B: "Electron-Hole Symmetry" in Achiral Nanotubes

It was stated that the Hamiltonian:

$$H_{0} = \sum_{j=1}^{J} \left[ \sum_{n=1}^{N} \epsilon_{jn} c_{jn}^{\dagger} c_{jn} + \sum_{n=1}^{N-1} c_{jn}^{\dagger} (t_{\parallel} + 2is\sigma_{j}) c_{j,n+1} + \sum_{n=1}^{N} c_{jn}^{\dagger} (t_{\perp} + 2i\mu\sigma_{z}) c_{j+1,n} + H.c. \right],$$

$$(4.9)$$

is invariant under the transformation:

$$c_{jn\uparrow} \to (-1)^{j+n} c_{jn\downarrow}^{\dagger}$$

$$c_{jn\downarrow} \to (-1)^{n+j+1} c_{jn\uparrow}^{\dagger}$$

$$c_{jn\downarrow}^{\dagger} \to (-1)^{j+n} c_{jn\uparrow}$$

$$c_{jn\uparrow}^{\dagger} \to (-1)^{j+n+1} c_{jn\downarrow}$$

when J is even or equal to 1. It is understood that if each of the parts of the Hamiltonian is invariant under the transformation, then the complete Hamiltonian is also invariant.

$$c_{jn}^{\dagger}c_{jn} = \begin{bmatrix} c_{jn\uparrow}^{\dagger}, & c_{jn\downarrow}^{\dagger} \end{bmatrix} \begin{bmatrix} c_{jn\uparrow} \\ c_{jn\downarrow} \end{bmatrix}$$
$$= c_{jn\uparrow}^{\dagger}c_{jn\uparrow} + c_{jn\downarrow}^{\dagger}c_{jn\downarrow}$$

Applying the transformation:

$$= (-1)^{j+n+1} c_{jn\downarrow} (-1)^{j+n} c_{jn\downarrow}^{\dagger} + (-1)^{j+n} c_{jn\uparrow} (-1)^{j+n+1} c_{jn\uparrow}^{\dagger}$$

$$= (-1)^{2(j+n)+1} c_{jn\downarrow} c_{jn\downarrow}^{\dagger} + (-1)^{2(j+n)+1} c_{jn\uparrow} c_{jn\uparrow}^{\dagger}$$

$$= -c_{jn\downarrow} c_{jn\downarrow}^{\dagger} - c_{jn\uparrow} c_{jn\uparrow}^{\dagger}$$

by applying the commutation rules of the creation and annihilation operators:  $\{c_i, c_j^{\dagger}\} = \delta_{ij}$ , it is possible to rewrite the result:

$$= c_{jn\uparrow}^{\dagger} c_{jn\uparrow} + c_{jn\downarrow}^{\dagger} c_{jn\downarrow} - 1$$

The spin-orbit term along the chain  $\sum_{j=1}^{J} \sum_{n=1}^{N-1} c_{jn}^{\dagger} (t_{\parallel} + 2is\sigma_{j}) c_{j,n+1}$  can be written in the matrix form:

$$t_{\parallel} + 2is\sigma_{j} = \begin{bmatrix} t_{\parallel} & 0 \\ 0 & t_{\parallel} \end{bmatrix} + 2is \begin{bmatrix} 0 & \sin\phi_{j} + i\cos\phi_{j} \\ \sin\phi_{j} - i\cos\phi_{j} & 0 \end{bmatrix}$$

recalling that  $\sigma_j = \sigma_x \sin \phi_j - \sigma_y \cos \phi_j$ .

$$= \begin{bmatrix} t_{\parallel} & -2se^{-i\phi_j} \\ 2se^{i\phi_j} & t_{\parallel} \end{bmatrix}$$

Then, it is possible to perform the multiplication with the creation annihilation operators:

$$\begin{split} &= \begin{bmatrix} c_{jn\uparrow}^{\dagger} & c_{jn\downarrow}^{\dagger} \end{bmatrix} \begin{bmatrix} t_{\parallel} & -2se^{-i\phi_{j}} \\ 2se^{i\phi_{j}} & t_{\parallel} \end{bmatrix} \begin{bmatrix} c_{jn+1\uparrow} \\ c_{jn+1\downarrow} \end{bmatrix} \\ &= \begin{bmatrix} c_{jn\uparrow}^{\dagger} & c_{jn\downarrow}^{\dagger} \end{bmatrix} \begin{bmatrix} t_{\parallel}c_{jn+1\uparrow} - 2se^{-i\phi_{j}}c_{jn+1\downarrow} \\ 2se^{i\phi_{j}}c_{jn+1\uparrow} + t_{\parallel}c_{jn+1} \end{bmatrix} \\ &= t_{\parallel}c_{jn\uparrow}^{\dagger}c_{jn+1\uparrow} - 2se^{-i\phi_{j}}c_{jn\uparrow}^{\dagger}c_{jn+1\downarrow} + t_{\parallel}c_{jn\downarrow}^{\dagger}c_{jn+1\downarrow} + 2se^{i\phi_{j}}c_{jn\downarrow}^{\dagger}c_{jn+1\uparrow} + H.c. \end{split}$$

$$= t_{\parallel} (c_{jn\uparrow}^{\dagger} c_{jn+1\uparrow} + c_{jn\uparrow} c_{jn+1\uparrow}^{\dagger} + c_{jn\downarrow}^{\dagger} c_{jn+1\downarrow} + c_{jn\downarrow} c_{jn+1\downarrow}^{\dagger}) + 2s$$

$$(-e^{i\phi_{j}} c_{jn\uparrow}^{\dagger} c_{jn+1\downarrow} - e^{i\phi_{j}} c_{jn\uparrow} c_{jn+1\downarrow} + e^{i\phi_{j}} c_{jn\downarrow}^{\dagger} c_{jn+1\uparrow} + e^{-i\phi_{j}} c_{jn\downarrow} c_{jn+1\uparrow}^{\dagger}) \quad (4.10)$$

Applying the transformation to this term:

$$\begin{split} &= \left[ (-1)^{j+n+1} c_{jn\downarrow} \ \, (-1)^{j+n} c_{jn\uparrow} \right] \left[ \begin{matrix} t_{\parallel} & -2se^{-i\phi_j} \\ 2se^{i\phi_j} & t_{\parallel} \end{matrix} \right] \left[ \begin{matrix} (-1)^{j+n+1} c_{jn+1\downarrow}^{\dagger} \\ (-1)^{j+n+2} c_{jn+1\uparrow}^{\dagger} \end{matrix} \right] \\ &= \left[ (-1)^{j+n+1} c_{jn\downarrow} \ \, (-1)^{j+n} c_{jn\uparrow} \right] \left[ \begin{matrix} (-1)^{j+n+1} c_{jn+1\downarrow} t_{\parallel} - (-1)^{jn+2} c_{jn+1\uparrow}^{\dagger} \\ 2e^{i\phi_j} (-1)^{j+n+1} c_{jn+1\downarrow}^{\dagger} + (-1)^{j+n+2} t_{\parallel} c_{jn+1\uparrow}^{\dagger} \end{matrix} \right] \\ &= (t_{\parallel} c_{jn\downarrow} c_{jn+1\downarrow}^{\dagger} + 2se^{-i\phi_j} c_{jn\downarrow} c_{jn+1\uparrow}^{\dagger} - 2se^{i\phi_j} c_{jn\uparrow} c_{jn+1\downarrow}^{\dagger} + t_{\parallel} c_{jn\uparrow} c_{jn+1\uparrow}^{\dagger} ) + H.c. \end{split}$$

After including explicitly the terms of the conjugate Hamiltonian, the expression is the same as the one in the equation. 4.10:

$$= t_{\parallel} (c_{jn\uparrow}^{\dagger} c_{jn+1\uparrow} + c_{jn\uparrow} c_{jn+1\uparrow}^{\dagger} + c_{jn\downarrow}^{\dagger} c_{jn+1\downarrow} + c_{jn\downarrow} c_{jn+1\downarrow}^{\dagger}) + 2s$$

$$(-e^{i\phi_{j}} c_{jn\uparrow}^{\dagger} c_{jn+1\downarrow} - e^{i\phi_{j}} c_{jn\uparrow} c_{jn+1\downarrow} + e^{i\phi_{j}} c_{jn\downarrow}^{\dagger} c_{jn+1\uparrow} + e^{-i\phi_{j}} c_{jn\downarrow} c_{jn+1\uparrow}^{\dagger})$$

The interchain spin-orbit coupling can be written in the matrix form:

$$c_{jn}^{\dagger}(t_{\perp} + 2i\mu\sigma_{z})c_{j+1n} =$$

$$= \begin{bmatrix} c_{jn\uparrow}^{\dagger} & c_{jn\downarrow}^{\dagger} \end{bmatrix} \begin{bmatrix} 2i\mu & 0 \\ 0 & -2i\mu \end{bmatrix} \begin{bmatrix} c_{jn\uparrow} \\ c_{jn\downarrow} \end{bmatrix}$$

$$= 2i\mu(c_{jn\uparrow}^{\dagger}c_{jn\uparrow} - c_{jn\downarrow}^{\dagger}c_{jn\downarrow} - c_{jn\downarrow}c_{jn\downarrow} + c_{jn\uparrow}c_{jn\uparrow}^{\dagger})$$

Applying the transformation:

$$= \begin{bmatrix} (-1)^{j+n+1}c_{jn\downarrow} & (-1)^{j+n}c_{jn\uparrow} \end{bmatrix} \begin{bmatrix} 2i\mu & 0 \\ 0 & -2i\mu \end{bmatrix} \begin{bmatrix} (-1)^{j+n}c_{jn\downarrow}^{\dagger} \\ (-1)^{n+j+1}c_{jn\uparrow}^{\dagger} \end{bmatrix}$$

$$= 2i\mu((-1)^{2(j+n)+1}c_{jn\downarrow}c_{jn\downarrow}^{\dagger} - (-1)^{2(j+n)+1}c_{jn\uparrow}c_{jn\uparrow}^{\dagger} + H.c)$$

$$= 2i\mu(-c_{jn\downarrow}c_{jn\downarrow}^{\dagger} + c_{jn\uparrow}c_{jn\uparrow}^{\dagger} + c_{jn\uparrow}^{\dagger}c_{jn\uparrow} - c_{jn\downarrow}^{\dagger}c_{jn\downarrow})$$